Correcting Parker Solar Probe electron measurements for spacecraft magnetic and electric fields

Daniel McGinnis[1], Jasper Halekas[1], Phyllis Whittlesey[2], Davin Larson[2], Justin Kasper[3]

[1]Department of Physics and Astronomy, University of Iowa, Iowa City, IA, USA
[2]University of California, Berkeley, Berkeley, CA, USA
[3]University of Michigan, Ann Arbor, MI, USA

Key Points:

- Spacecraft-produced electrostatic and magnetic fields interfere with the collection of PSP SPAN-E data
- These fields are modeled in order to estimate how electron measurements are affected
- A technique for correcting electron measurements using these results is presented

This is the author manuscript accepted for publication and has undergone full peer review but has not been through the copyediting, typesetting, pagination and proofreading process, which may lead to differences between this version and the Version of Record. Please cite this article as doi: 10.1029/2019JA026823

Corresponding author: Daniel McGinnis, daniel-mcginnis@uiowa.edu

Abstract

The spacecraft body of the Parker Solar Probe may interfere with electron measurements in two ways. The first is the presence of several permanent magnets near the SPAN instruments. The second is the widely varying spacecraft potential. We estimate the effect of these interferences by performing particle tracing simulations on electrons of various energies using a simplified model of the spacecraft potential and measurements of the magnetic fields. From this we can 1) estimate the individual and combined fields of view of the SPAN-E instruments 2) identify regions of phase space which may be highly distorted and 3) simulate measurements of the velocity distribution function. We compute density, temperature, and bulk velocity moments of the measured distribution functions and find that a correction table derived from the particle tracing results can be incorporated in the computation to greatly decrease the errors caused by the spacecraft potential and magnetic fields. Similar tables could be computed for a wide range of spacecraft potentials and applied during the processing of actual SPAN data.

1 Introduction

Accurate in situ measurements require unaltered sampling of the surrounding space plasma. Unfortunately, the spacecraft itself is often a source of interference, so understanding how it impacts the operation of onboard instruments is important so that its effects can be anticipated and corrected. In contrast to the measurement of electric or magnetic fields, particles are typically measured by instruments located near the spacecraft body and are thus subject to a) blockages in field of view (FOV) from the body or other components of the spacecraft and b) the close proximity to the various electromagnetic fields produced on or by the spacecraft. The effects of these fields on the measurements depend on the magnitude of the spacecraft potential and permanent magnetic fields and their spatial distribution around the spacecraft. In this work, we use a simple model of the Parker Solar Probe (PSP) spacecraft and the electric and magnetic fields around it to estimate how the instrumental FOV and measurements of the electron distribution function might be affected.

Particle measurements are taken by the Solar Wind Electrons Alphas and Protons (SWEAP) investigation, a suite of instruments composed of the Solar Probe Cup (SPC), a Sun facing Faraday cup, and the 3 electrostatic analyzers (ESAs) of the Solar Probe Analyzers (SPAN) suite (Kasper et al., 2016). SPAN-A is made up of an ion (SPAN-i) and an electron (SPAN-Ae) ESA located on the ram side of the PSP, while SPAN-B is another electron ESA on the anti-ram side of the spacecraft. The fields of view of the SPAN-Ae and SPAN-B instruments are complementary, providing almost complete coverage of the sky, except for the region blocked by the Sun facing heat-shield and the SPC (Kasper et al., 2016). The SPAN-Ae and SPAN-B instruments (collectively referred to as SPAN-E) determine bulk properties of solar wind electrons by sampling the electron velocity distribution function (eVDF) in the energy/charge range of several eV/q to 20keV/q. Scientifically important plasma properties, such as density, temperature, and velocity can then be computed from these eVDF measurements.

The accuracy of these measurements are likely degraded by the electromagnetic fields produced by the spacecraft. Several permanent magnetic field-producing spacecraft components are located in close proximity (within about 1 m) to the SPAN ESAs. The combined strength of these fields (a few nT or more) is likely to cause aberration in electron trajectories, so that the electrons are measured by the ESAs at different directions than their velocity vectors in the ambient plasma. In aggregate, this causes a non-uniform "warping" of the eVDF in the directions where the combined magnetic field is greatest.

In addition to the magnetic fields, the electrostatic charging of the PSP impacts the measurement of solar wind electrons. The magnitude of this impact is dependent on the magnitude of the spacecraft potential, which is likely to vary over the lifetime of the

PSP's mission. The charges which create the spacecraft potential, Φ_{SC}, are delivered by currents. The most important of these are due to the production of photoelectrons, the collection of ambient electrons, and the production of secondary electrons (Whipple, 1981; Garrett, 1981; Lai, 2011). The strength of the first two of these is determined by quantities which vary with heliospheric distance: photoelectron current varies with solar UV photon flux and the ambient electron current depends on local plasma properties such as density and temperature. Therefore, the potential to which a spacecraft may charge is dependent on its distance to the Sun. At 1AU, conditions are such that spacecraft in the solar wind typically charge to a benign few volts positive (Whipple, 1981).

PSP used a series of Venus gravity assists to lower its perihelion from $35R_s$ to within $10R_s$ (0.044 AU) (Fox et al., 2016). At these heliospheric distances, conditions in the solar wind allow for negative spacecraft potentials to develop. Ergun et al. (2010) incorporate detailed physics describing the production of photo-, thermal, and secondary electron currents to numerically solve for the electrostatic potential structure surrounding a simplified model of the PSP. They find that at $\sim 10R_s$, an enhanced photoelectron density near the spacecraft surface can create an electrostatic barrier which reflects currents of photoelectrons back to the spacecraft if the Debye length of these electrons is small. Currents of ambient electrons can penetrate through this barrier if their thermal energy is large compared to the characteristic energy of the photoelectrons. The sum of these currents causes the spacecraft to charge to negative potentials and the presence of an ion wake further reflects currents of photoelectrons and secondary electrons, leading to a much more negative potential. Depending on the yield of secondary electrons, the spacecraft charges from a few volts negative to as much as $\Phi_{SC} \sim -kT_e \approx -85V$. Guillemant et al. (2012) find qualitatively similar results with a modified version of the code used in Ergun et al. (2010) and using the SPIS 3D particle in cell software, they found the spacecraft settles to potentials typically between -10V and -20V. A similar procedure is repeated for different heliospheric radii in Guillemant et al. (2013), who find that PSP charges more negatively than -5V only at distances less than 0.067AU, reaching -16.23V at $9.5R_s$.

Depending on the relation between the signs of the particle charge, q and Φ_{SC}, spacecraft potential either increases (opposite sign) or decreases (same sign) the kinetic energy of measured particles by an amount $q\Phi_{SC}$. If the signs are opposite, no ambient particles are measured at energies less than $q\Phi_{SC}$, since all particles have been accelerated by this amount in the potential. In this case, any electrons measured below this energy are primarily returning photo- and secondary electrons, a fact which can be used to determine the value Φ_{SC} (Johnstone et al., 1997; Rymer, 2004). Conversely if the signs are the same, as with electrons and a negative spacecraft, particles with energies less than $q\Phi_{SC}$ cannot reach the detector and the corresponding portion of the distribution function will not be measured. Additionally, the electric field of the spacecraft bends trajectories of particles incident on a detector. For spherically symmetric potentials, this bending is symmetric with respect to the center of the detector, so that the same average look direction is measured. However, due to the focusing effect of the attractive potential, trajectories of electrons converge as they near a positive potential. This means that the angular coverage of the detector increases and a wider element of phase-space is being measured (Lavraud & Larson, 2016).

Several methods have been described to correct electron and/or ion measurements for spacecraft potential. Briefly, (see Lavraud and Larson (2016) for a more thorough review), these often assume a Maxwellian plasma distribution and a spherical potential in order to find conversions between the measured and real moments. These conversions have been found by direct modification to the analytic form of the moment integrals to account for the low energy cutoff (Song et al., 1997), the development of a correction model informed by comparing field and particle data (Salem et al., 2001), or numerically inverting the system of equations with unknown potential (Génot & Schwartz, 2004). Al-

ternatively, correcting for only the potential energy shift can be done without the need to first assume a model plasma distribution. Lewis et al. (2008) correct Cassini CAPS-ELS electron count measurements for spacecraft potential by converting to phase space density, shifting the energy scale by an amount corresponding to the potential, then converting back to counts before comparing plasma moments determined via integration and model fitting. Lavraud and Larson (2016) justify the theoretical basis for this conversion in terms of Liouville's theorem and prescribe its usage in the calculation of the moment integrals. Without any dependence on models, the accuracy of the plasma moments obtained via integration is dependent on obtaining as complete a coverage of the full distribution as possible. A separate method is still required to estimate the portion of the spectrum that is not measured below the energy cutoff and if the full 4π sr solid angle of the sky is not covered.

However, the nonradial forces imparted on measured plasma particles by the permanent spacecraft magnetic fields, along with the roughly cylindrically symmetric electrostatic potential structure found by detailed modeling (Ergun et al., 2010; Guillemant et al., 2012, 2013), suggest that the spherical potential assumption used in the above techniques may not be valid for PSP. Determining analytically how trajectories bend through non-spherical potentials, and the corresponding angular corrections, can instead be done using numerical methods (Isensee, 1977; Scime et al., 1994; Hamelin et al., 2002). (Isensee, 1977) study the effect of the Helios spacecraft on the measurement of electron velocity distribution functions in the inner heliosphere (0.2 AU). They used a particle-in-cell method to estimate the two-dimensional electrostatic potential structure surrounding the spacecraft by self-consistently tracing the density and trajectory of an initial distribution of electrons representing the solar wind. Also included in the simulation were a bulk flow of solar wind ions and the production of photoelectrons by sunlit spacecraft surfaces. The simulation showed that the spacecraft settles at a potential of 2.9V and is surrounded by regions of negative potential in both the sunward and antisunward-facing directions, due to the buildup of photoelectrons and the absence of ions in the ion wake, respectively. The effect of these regions on electron measurements was then demonstrated by showing sample electron trajectories with various initial velocity angles and kinetic energies: at lower energy (near the spacecraft potential), electrons can be reflected by the potential minima, while at slightly higher energy (up to about 20 eV), electron trajectories can be shifted in angle considerably.

Using the form of the potential surrounding a charged infinite plane, Scime et al. (1994) derive an expression for the electron velocity angle far from the spacecraft in terms of its velocity angle close to the spacecraft, the spacecraft potential, and the electron energy. The NASA/Air Force Spacecraft Charging Analyzer Program (NASCAP (Katz et al., 1977; Mandell et al., 2006)) was used to reconstruct the electrostatic potential structure surrounding a moderately detailed model. The same program was used to trace particle trajectories at different angles originating from the location of the Ulysses Solar Wind Plasma Experiment's electron spectrometer. At the finest resolution scale allowed by the code (still many times larger than the photoelectron sheath Debye length), the particle trajectories were confirmed to be closely approximated by the plane-parallel solution. The plane-parallel function was used to correct for the true look direction of each detector in the instrument (the center trajectory). In addition, the solid angle coverage of each detector was corrected at each energy with a spacecraft potential dependent correction to the geometric factor of the instrument determined by calculating the corrected total angular acceptance. With these corrections, they were able to reduce the disagreement between the ion and electron instrument's measurement of the solar wind speed from 14% to 2%.

Hamelin et al. (2002) compute the electrostatic potential surrounding a model of the auroral satellite Interball-2 in order to trace the stochastic variations in ion trajectories within each measurement window of the on-board Hyberboloid multi-directional

ion mass spectrometer (Dubouloz et al., 1998). Using these results, they apply a correction for the angular distortions in the flux measurements caused by the potential by deriving probability maps of the actual angles from which ions measured in each window originated.

In this paper, we investigate how the spacecraft electrostatic and magnetic fields affect SPAN electron measurements. Similar to previous studies, we perform a particle tracing analysis to determine electron trajectories influenced by a simple approximation of the potential structure around PSP. We do this for a series of spacecraft potentials spanning the range of possible values predicted in the literature. We additionally include a measurement driven model for the magnetic fields produced by PSP and a simple model of the spacecraft body. In Section 2 we detail the spacecraft model and potential, the magnetic field model, and the particle tracing simulation. In Section 3, we describe how the particle tracing results were used to synthesize measurements of a known distribution function as viewed through these fields. To do this, we removed potentially bad or problematic data (Section 3.1), then combined the SPAN-Ae and SPAN-B measurements (Section 3.2), and discuss how the effects of the fields may be corrected (Section 3.3). We quantify how the field of view of each instrument is affected in terms of individual pixels in Section 4.1 and in terms of angular coverage of the sky in Section 4.2. We demonstrate how well measurements of the distribution function moments are recovered with and without the use of our correction scheme in Section 4.3. Results are discussed in Section 5, and lastly we conclude in Section 6.

2 Procedure

To what degree the electron measurements are impacted by the magnetic fields produced in close proximity to the SPAN instruments, as well as by the wide range of possible spacecraft potentials, is largely unknown. Determination of the magnitude of these effects was of primary importance in the present study, along with the development of a method of correcting for their gross features. Thus several simplifications to the models (such as neglecting the ion wake (Isensee, 1977; Ergun et al., 2010) in the spacecraft potential) were made in order to facilitate the investigation of a wide range of spacecraft potentials.

2.1 Spacecraft Potential Model

The body of the PSP spacecraft was modeled to aid in the calculation of the space potential around the spacecraft and to provide an updated estimate of the field of view of the instrument. In order to simplify our calculations, we approximated the spacecraft as a 1.0m diameter by 1.69m long cylinder connected to a 1.31m long cone segment with a 2.3m outer diameter. The model was composed of 40,400 points arranged by rotating about the cylindrical axis the points forming one boundary edge.

In order to estimate the effects of the spacecraft potential on the charged particle measurements, rough calculations of the electric field surrounding the spacecraft were computed for a number of spacecraft potentials and Debye lengths of the surrounding plasma. The electric field was assumed to be cylindrically symmetric about the spacecraft $\widehat{z}$ axis in order to save calculation time. This 2-dimensional slice of the simulation space was subdivided into a rectangular grid of 14,400 6cm×12.5cm cells, extending 6m from all spacecraft surfaces. It was assumed that all spacecraft surfaces are conductive and have the same potential Φ_{SC} and that the potential of the surroundings approximately followed the form of a modified Debye potential such that the electric field can be calculated using

$$E(\rho, z) = \frac{\Phi_{SC}}{\lambda_D} \exp\left(-\mathbf{r}/\lambda_D\right) \widehat{\mathbf{r}} \tag{1}$$

where $\mathbf{r}$ is the distance from the field point to the nearest element on the body of the spacecraft, and the normalized vector $\widehat{\mathbf{r}}$ points along this direction. The Debye length, λ_D, will in general be affected by photoelectrons produced on sunward facing surfaces, however, we have assumed that λ_D remains constant across our simulation space. To first order, this should have minimal impact on our analysis since electron trajectories in our simulations rarely extend into the Sun-exposed regions of our model (*i.e.* in front of the heat shield).

2.2 Magnetic Field Model

The known magnetic sources include the traveling-wave tube amplifiers (TWTAs), latch valves, RF switches, and propulsion thrusters. The static DC magnetic fields surrounding each of these components have been individually measured and their magnetic moments and locations in spacecraft coordinates were made available to us. The magnetic field at a location, $\mathbf{r}$ in our simulation space was calculated using the superposition of the magnetic fields produced by each spacecraft component,

$$B(\mathbf{r}) = \frac{\mu_0}{4\pi} \sum_i \frac{3\mathbf{r}' \left(\mathbf{m}_i \cdot \mathbf{r}'\right)}{|\mathbf{r}'|^5} - \frac{\mathbf{m}_i}{|\mathbf{r}'|^3} \tag{2}$$

with $\mathbf{r}' = \mathbf{r} - \mathbf{R}_i$, the distance from magnetic field source located at $\mathbf{R}_i$ and where $\mathbf{m}_i$ is the magnetic moment of the source.

2.3 Particle Tracing

The effect of these fields on electron measurements was determined by simulating the particles' trajectories as they move (backwards in time) from their detection at the instrument location outwards. In our simulation, electrons were started at either SPAN-Ae or SPAN-B with a given kinetic energy and initial velocity angle, then their positions were calculated at a series of time steps of duration equal to 10^{-3} times the electron's local gyro-period. The simulation advances by approximating the solution to the Lorentz force equations of motion using a fourth-order Runge-Kutta method algorithm. The simulation terminates when the electron has traveled either back to or effectively far (>6m) from the spacecraft.

Each of the SPAN electron instruments has eight high-resolution 6° anodes and 8 low-resolution 24° anodes which each integrate flux at 32 elevation angles. Each anode has some width in azimuthal angle, and each measurement bin has some spread in elevation angle, so each measurement point in angular space has some finite collection area, forming a measurement pixel with 4 corner vertices. In the coordinate frames where $\hat{\phi}$ and $\hat{\theta}$ (the azimuthal and elevation angles, respectively) are measured with respect to the orientation of each instrument, measurement points are regularly spaced and these pixels are rectangular. When rotated into the coordinate frame of the spacecraft, these pixels are warped into curved shapes (see the top and bottom panels of Figure 1). By tracing the particle trajectories of the electrons with initial velocity angles corresponding to each of these 4 corner vertices as they travel outward from the spacecraft, we are able to estimate each pixel's field of view (FOV) coverage of the surrounding plasma. This FOV is defined as the area in ϕ, θ swept out by these final velocity angles, connected by borders similarly warped to the spacecraft coordinate system.

At least 3 of the final velocity angles are needed to define an area of the solid angle FOV. Therefore, any pixel that has two or more closed trajectories (those which end on the spacecraft when traced from the instrument outward) is considered completely blocked and was removed from further analysis. If only one trajectory of a pixel is blocked, it is removed and the FOV area is determined from the remaining 3.

Simulations were performed at each pixel corner vertex for electron kinetic energies (measured at the detector) in 5eV increments from 15-110eV, in 20eV increments from 130-350eV, and 50 eV increments from 360-510eV (34 energies). The latter two increments were widened to save on processing time and because the electron trajectories become successively less affected with increased kinetic energy. The simulations were done for model spacecraft potentials of -85V, -25V, -15V, -10V, -5V, 0V, +5V, and +10V. Following Ergun et al. (2010), who found that one of the necessary conditions for negative Φ_{SC} is $\lambda_{Dph} \ll R_{SC}$, (where λ_{Dph} is the Debye length of the photoelectrons, and R_{SC} is the size scale of the spacecraft), we used Debye lengths of 0.15 m and 1 m for the negative and positive potential models, respectively. Lastly a set of reference simulations were run with $\Phi_{SC} = 0$ and no magnetic field.

3 Synthetic Measurement

The results of the particle tracing simulation can be used to estimate what measurements of a known electron velocity distribution function (eVDF) might look like through the effects of the warping fields. In order to do this, a bi-Maxwellian electron distribution representing the pristine plasma far from the spacecraft was first created. This distribution was computed using a -400 km s^{-1} velocity antisunward (the $+\hat{x}$ direction in the spacecraft coordinate frame) and temperature values roughly approximating the environment at $10R_\odot$: $T_\perp/T_\parallel = 3$ and $T_{\rm avg} = 1{\rm MK} (\approx 85{\rm eV})$. The suprathermal electron populations typically seen in the solar wind, the halo and the strahl, were not included. Although of scientific importance, they are characterized by higher thermal energies (10^2 to 10^3) and would be subsequently less affected by the spacecraft fields. Values of the energy flux were calculated at 1° increments from $-90° \leq \theta \leq 90°$ and $-60° \leq \phi \leq 300°$ and over the energy range 5-510eV in 5eV increments.

The FOV of each pixel that was determined from our tracing simulations is the solid angle over which that pixel receives electrons from the surrounding plasma. Consequently, we estimate the electron energy flux measured at energy E_m by first locating the ϕ, θ values of our eVDF within the warped FOV of each pixel. We then take the mean of the energy fluxes of these eVDF points at the ambient energy, $E_a = E_m + q\Phi_{SC}$, in order to account for the effect of the spacecraft potential, Φ_{SC} on the electron energy. Lastly, the result is scaled by $(1+q\Phi_{SC}/E_m)^{-2}$ to account for the effect of the spacecraft potential on the energy flux.

Complete measurement sets were composed by repeating this process for all pixels and for measured energies in the range $E_m = 15 - 510$eV at 5eV steps. Since our particle tracing simulations were performed at variable increments over this range, the closest simulation results were used when there were no data at the corresponding energy. Finally, we remove data for which $E_m < |q\Phi_{SC}|$, since this is the minimum energy electrons can have after accelerating through positive spacecraft potentials and the minimum energy measureable for negative potentials.

3.1 Data Quality Flagging

In an idealized detector with a spherical (or nearly) electrostatic potential, no ambient magnetic field, and full 4π sr FOV (*e.g.* Scime et al. (1994); Génot and Schwartz (2004); Lavraud and Larson (2016)), the deflection of electron trajectories varies smoothly with measurement angle and all data is perfectly usable. The more complex field structures combined with blocked FOV regions in the current study make determination of accurate plasma moments more challenging. We have developed two selection criteria to flag for exclusion the measurement bins which are potentially the most detrimental.

The first of these flags the electron trajectories which are deflected by too large of an angle between initial and final velocity direction in the tracing simulation. These tra-

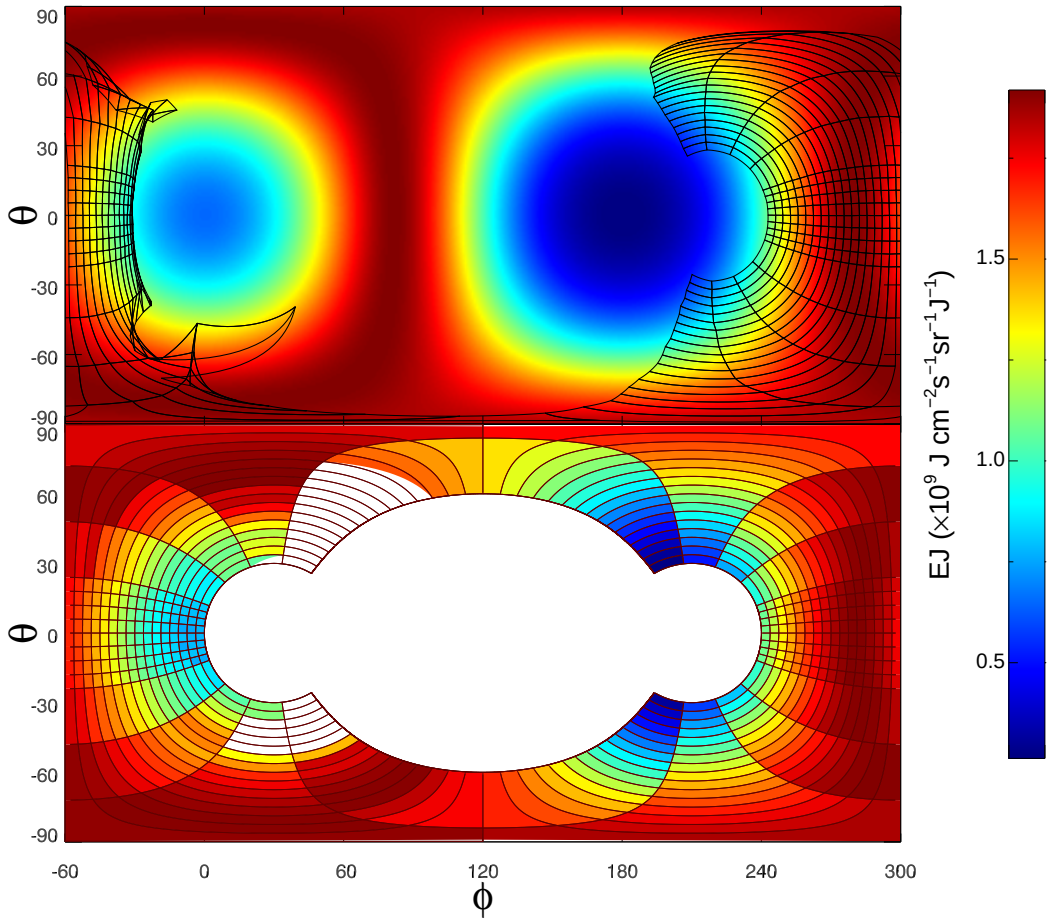

Figure 1. Illustration of the creation of a synthetic measurement set for SPAN-B. By tracing electron trajectories from the corners of each instrument measurement pixel outward under the influence of the magnetic and electrostatic fields, we obtain the angular region of the velocity distribution function (VDF) that is sampled by that pixel (wire outlines, top panel). The average of the energy flux within this region is then the measurement at the original pixel location (bottom panel). Because of the effects of the fields on the electron trajectories, several pixels are blocked by the spacecraft (white regions) and the measured VDF (color scale, bottom panel) is distorted from the actual VDF far from the spacecraft (color scale, top panel).

jectories are nearly always clustered in small regions in angle space, suggesting they have a localized cause (*e.g.* an abrupt polarity change in the local magnetic field) and are not produced by our smoothly-varying electrostatic potential model. Measurement pixels associated with these trajectories sample much different regions of the surrounding eVDF than neighboring pixels, with the magnitude of this discontinuity dependent on the average deflection angle. The maximum deflection angle was determined using the expression derived in Scime et al. (1994) for a particle traveling through a 2D spacecraft potential with different strengths in each dimension. Assuming the potential is equal in both directions, we obtain an upper limit of 45° using the minimum ambient electron energy (15eV) and the maximum spacecraft potential (-85V) that was modeled. To further avoid the possibility of removing usable data, we raise this upper limit by 15°. Thus, any bin which has a geometric center that is deflected more than 60° by our model fields is flagged.

Second, since the angular coverage of each pixel is nominally less than 24° along each axis, pixels which spread by more than 45° in any direction at the end of the tracing were flagged since the energy fluxes are being averaged over too wide of a region of a VDF. Pixels meeting either one of these conditions were removed in Figure 1, and along with the pixels blocked by the spacecraft, lead to a large space of the eVDF that is not measured at $\theta = +45°$ to $+90°$ in the top panel.

3.2 Combining SPAN-Ae and SPAN-B Data

The SPAN-Ae and SPAN-B electron detectors are on opposite sides of the PSP, simultaneously measuring complementary regions of the sky. This placement, while providing a nearly full FOV, causes challenges to the computation of the moments of the electron distribution function. Since the distribution function, $f(\mathbf{r}, \mathbf{v})$ is sampled by accumulating electron counts in discrete bins of velocity, $v \pm \Delta$v, (or energy, $E \pm \Delta E$), azimuthal angle $\theta \pm \Delta\theta$, and elevation angle $\phi \pm \Delta\phi$, the moment integrals are converted into discrete sums. For example, following Lavraud and Larson (2016), the total number density moment integral, $N = \int f d^3$v, rewritten in spherical coordinates using $d^3v = v^2 dv \cos\theta d\theta d\phi$, (where the trigonometric function $\cos\theta$ is used since the angle θ is the latitude measured from -90° to 90°), and using the instrumental geometric factor

$$G = \frac{C}{f v^4} \tag{3}$$

to convert the distribution function f to particle counts, C,

$$N = \frac{1}{G} \int \frac{C}{v^2} \mathrm{d}v \cos\theta \mathrm{d}\theta \mathrm{d}\phi. \tag{4}$$

which can be transformed into a sum over the product of the average value of the cosine of the elevation angle latitude, $< \cos\theta >$ with the count rate in each bin, C_{ijk}

$$N = \frac{1}{G} \sum_{v_i} \frac{\Delta v}{v^2} \sum_{\phi_k} \sum_{\theta_j} < \cos\theta > C_{ijk} \, \Delta\theta_j \, \Delta\phi_k \tag{5}$$

In the coordinate systems originating at and normal to their centers, each instrument measures the eVDF in a regular grid in v, θ, and ϕ; thus the values of Δv, $\Delta\theta_j$, and $\Delta\phi_k$ are well defined for each instrument in this frame. However, the rotational transformations necessary to map these grids from one instrument's coordinate system to the other's, or onto any common frame (*e.g.* the spacecraft coordinate system), distort the regular spacing between the measurement points. In such a collection of irregularly spaced measurement points, the values of θ_j and ϕ_k are ill-defined. Therefore, the moment calculations must either (1) be performed separately for each instrument in its own coordinate system, then the results combined, or (2) the data must be resampled so that the values $(\Delta\theta_j, \Delta\phi_k)$ can be determined. The first of these two options would require some method of accounting for the overlap in instrument FOVs. For the density moment, this may be a simple scaling factor, but becomes more difficult for the higher-order moments, especially as the amount and location of the overlap in FOV changes with spacecraft potential. The second option is preferred since it allows calculation of the eVDF moments using data from both instruments simultaneously and allows for the straightforward handling of FOV overlap via averaging (next paragraph). We resample our synthetic data sets by using a thin-plate-spline algorithm (essentially a 2D cubic spline) to interpolate separately the measurements taken by each instrument at each energy to a regular grid spanning the full sky ($-90° \leq \theta \leq 90°, -60° \leq \phi \leq 300°$) at $5° \times 5°$ resolution. We then remove the points in the interpolation which extend beyond the angular coverage of the actual instrument FOV determined from our tracing simulations. The two datasets were then combined into one, taking the mean of the energy flux values where there is a measurement at the same location in both datasets. The remaining gaps in the total FOV coverage were removed by performing a second interpolation at each energy in the combined data set using the same algorithm and resolution as the first.

3.3 Correcting for E and B Fields

It is during this step of the data processing that we may attempt to correct for the warping effect of the spacecraft electrostatic and magnetic fields. The interpolation routine requires the input data to be assigned a set of (ϕ, θ) coordinates. By using the nominal look direction of each instrument bin's center for these coordinates, we are assuming that the effect of the fields is negligible and that the eVDF of the ambient plasma is actually sampled at these directions. Any warping (stretching, compressing, translations, etc.) in the eVDF measurement caused by these fields will be incorporated into the interpolation. Alternatively, from the results of the particle tracing, we know the angles at which the ambient plasma was actually sampled. By replacing the nominal instrument bin directions with these angles, the warping is rectified, and the resulting interpolation is a much more accurate representation of the plasma eVDF.

For the set of synthetic measurements created for each spacecraft potential, we compute the density, temperature, and velocity moments of a raw (uncorrected) and a corrected data set. In contrast to the uncorrected sets, the corrected sets had potentially problematic data flagged and removed. Additionally, the angular coordinates measured in the eVDF were used in the interpolation and data points outside of the actual FOV were removed after the interpolation. A second round of interpolation was then done to remove gaps in the coverage of the final combined FOV. Measurement of the density, temperature, and bulk velocity plasma moments was performed using modified versions of routines created for the software development platform SPEDAS (Space Physics Environment Data Analysis Software (Angelopoulos et al., 2019)). Measurement of the heat flux, related to the third-order moment of the eVDF, while a scientifically useful quantity, was not computed since it is less affected by changes at lower energy, where the effect of the spacecraft potential and magnetic fields are highest. The spacecraft potential was accounted for by multiplying the energy flux at each energy, E_m by the $\left(1 + \text{sign}(q)\frac{e\Phi}{E_m}\right)^{\frac{N+1}{2}}$ correction factor described by Lavraud and Larson (2016), where N is the order of the moment of the distribution that is calculated.

4 Results

As mentioned, the aim of the present study is to quantify the effect on SPAN electron measurements from spacecraft magnetic fields and electrostatic charging and to subsequently develop a method of correcting for these effects. While representing an improvement over the assumptions of a zero-size spacecraft surrounded by a spherical potential with no onboard magnetic fields, the following results are still intended to provide an order of magnitude estimation of this effect. Although the details of the results in this section are model dependent, our correction technique is not.

4.1 Pixel Blockage and Data Quality

In our particle tracing simulation, the trajectories for each of the 512 pixels (16 anodes at 32 azimuthal angles each) are computed at 34 (measured) electron kinetic energies. Each instrument therefore has 17,408 total measurement bins. The fraction of the total number of bins that are fully blocked, i.e. have 2 to 4 closed pixel corner trajectories blocked, is shown in Table 1. The number of partially blocked bins is roughly a constant fraction of the number of fully blocked bins (≈10% for SPAN-Ae and ≈20% for SPAN-B) and is not shown.

In the absence of any fields (the No E/B column), our crude spacecraft model fully blocks 1870 of SPAN-Ae's bins (≈11% of the total) and 2142 of SPAN-B's (≈12%). Including the magnetic field to the 0V spacecraft potential (the 0V column) had a negligible effect on the fraction of blocked SPAN-B bins, while nearly doubling the amount of fully blocked bins in SPAN-Ae. The fraction of fully blocked bins increased by about

Table 1. Percentage of the total number of measurement bins, across all energies, that are either fully blocked (have 3 or 4 blocked trajectories, top two rows) or have been removed to improve data quality (bottom two rows, see Section 3.1 for removal criteria).

	No E/B	**+10V**	**+5V**	**0V**	**-5V**	**-10V**	**-15V**	**-25V**	**-85V**
% Fully (Ae)	10.7	21.1	19.9	18.9	16.6	16.0	15.6	15.0	12.4
% Fully (B)	12.3	14.6	13.3	12.2	8.8	7.0	6.1	4.7	2.0
% DataQ (Ae)	0.0	2.0	1.2	0.9	1.0	0.7	0.5	0.4	2.2
% DataQ (B)	0.0	3.3	3.1	2.9	1.3	1.0	0.8	1.0	4.2

a percent for both instruments as the potential increased from 0V to +5V, and another percent from +5V to +10V. Fewer bins were blocked at all negative potentials, with the fractional amount decreasing with potential. It is worth noting, however, that at negative spacecraft potentials, fewer pixels blocked does not necessarily relate to greater coverage of the sky (see Section 4.2). In all models except No E/B, fewer of the SPAN-B instrument bins are blocked than for SPAN-Ae.

The number of bins that we have flagged and removed for potentially poor data quality is also shown in Table 1, as a fraction of the remaining (non-blocked) bins. The fraction flagged is zero for the No E/B case, since our criteria revolve around large trajectory changes, which do not occur without fields. By itself, the inclusion of the magnetic field caused ≈1% of the SPAN-Ae and ≈3% of the remaining SPAN-B bins to be flagged and removed. Positive potentials increased these fractions and negative potentials decreased them except for the -85V model, which had the highest fractions removed for each instrument (2.2% and 4.2% for Ae and B, respectively). In contrast to the fraction of blocked bins, SPAN-B had more flagged bins across all models. For both instruments, the flagged pixels occur preferentially at lower energies, as the trajectories of higher energy electrons are less affected by the fields.

We show the locations of the pixels which are most often blocked (left panels) or flagged (right panels) in Figure 2. The heavy line indicates the region blocked by our spacecraft model alone (Φ_{SC}=0,B=0). Our simulations show that a large number of SPAN-Ae's measurement bins experience blockage from $145^\circ \lesssim \phi \lesssim 250^\circ$ at all elevation angles, corresponding to the trajectories skimming along the anti-sunward edge of our spacecraft model. As discussed in the next section, the amount of blockage in this region is likely overestimated by the geometry of our spacecraft model. The SPAN-B bins that are blocked are mainly gathered at $-15^\circ \lesssim \phi \lesssim 125^\circ$ at the elevation angles relating to the trajectories nearest the spacecraft. These are also largely the same pixels blocked in the $\Phi_{SC} = 0$ and $\Phi_{SC} = 0, B = 0$ models. In both maps, the pixels near $\phi = 0, \theta = 0$ look sunwards along the spacecraft body towards the thermal protective system heat shield. The heat shield of our spacecraft model blocks 10 of SPAN-Ae's pixels, and approximately 4-5 times that amount of SPAN-B's pixels.

Almost all of the SPAN-Ae bins that were flagged (top panel, Figure 2) lie either in the small area from $5^\circ < \phi < 15^\circ, +20^\circ < \theta < 35^\circ$ or the pixel at $\phi = 255^\circ, \theta = +45^\circ$, while those for SPAN-B (bottom panel) are found in two looser groupings from $-25^\circ < \phi < 45^\circ$ at $+20^\circ < \theta < +60^\circ$ and $-65^\circ < \theta < -30^\circ$. In Figure 3, we calculate the x, y, z, components and total magnitude of the magnetic field surrounding the spacecraft (shown as a white circle, the location of SPAN-A is represented with a line connected to the spacecraft, while SPAN-B is represented as a line that is not) over a slice perpendicular to the spacecraft axis, located 0.50 m from the anti-sunward facing end. In this coordinate system, $+z$ runs along the center of the long axis of the spacecraft, pointing towards the Sun, $+x$ points in the ram direction, and $+y$ completes the right

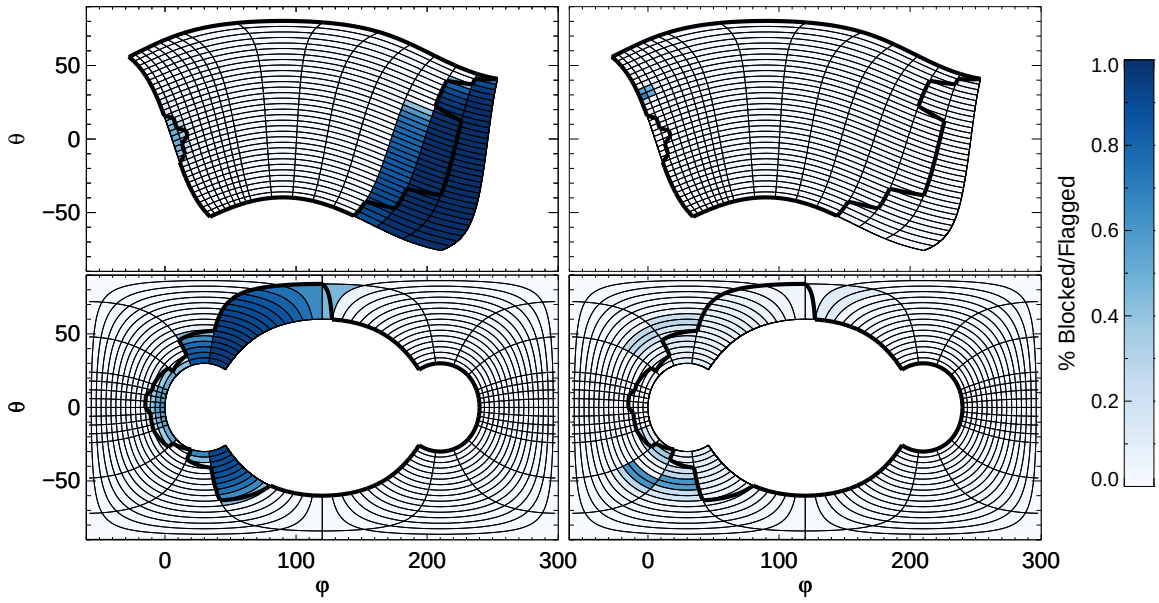

Figure 2. Heatmap of the measurement bins most often blocked (left panels) and flagged for potentially poor data quality (right) for all models except the No E/B model. The bins of the SPAN-Ae instrument are shown in the top panels and the SPAN-B instrument are shown in the bottom panels. The dark outline represents the region of each instruments' field of view that is blocked by our representation of the PSP.

handed set. Overplotted are lines representing the look direction in this plane of the pixels which were most often flagged for SPAN-Ae (top left) and SPAN-B (top right). In each of the component maps, there are several locations near the spacecraft where the field abruptly reverses to an opposite polarity at approximately the same magnitude.

The group of lines extending towards the -y direction in the top left panel of Figure 3 travel through a region of sharp reversal in B_z. The lines also correspond to the look directions of the most flagged SPAN-Ae pixels, suggesting the magnetic field structure is at least partially responsible for the pixel flagging. Although there are likely no SPAN-B pixels which do not see any magnetic field discontinuities along their line of sight, those extending towards $+y$ (in the $-\theta$ direction in Figure 3) look through polarity switches in B_x, B_y, and to a small extent B_z, while those in the $-y$ direction, ($+\theta$), see the flip in the sign of B_y near the instrument, and the flip of B_x and B_z a little further from the instrument.

4.2 Instrument FOV

Due to the electrostatic and magnetic fields, the solid angle areas of the instrument pixels do not necessarily correspond to phase space elements along these directions in the plasma while maintaining the same angular extent. Thus, while Table 1 and Figure 2 give an indication of how many and which instrument bins might receive either diminished or severely mislocated electron energy flux, they cannot be used to directly determine how the instrumental FOV is affected by our model fields.

To estimate this behavior, the areas of the sky measured by the individual pixels (i.e. the "warped" pixels, top panel, Figure 1) were combined into a single region at each measured energy. The regions for the individual SPAN-Ae and SPAN-B sensor FOVs

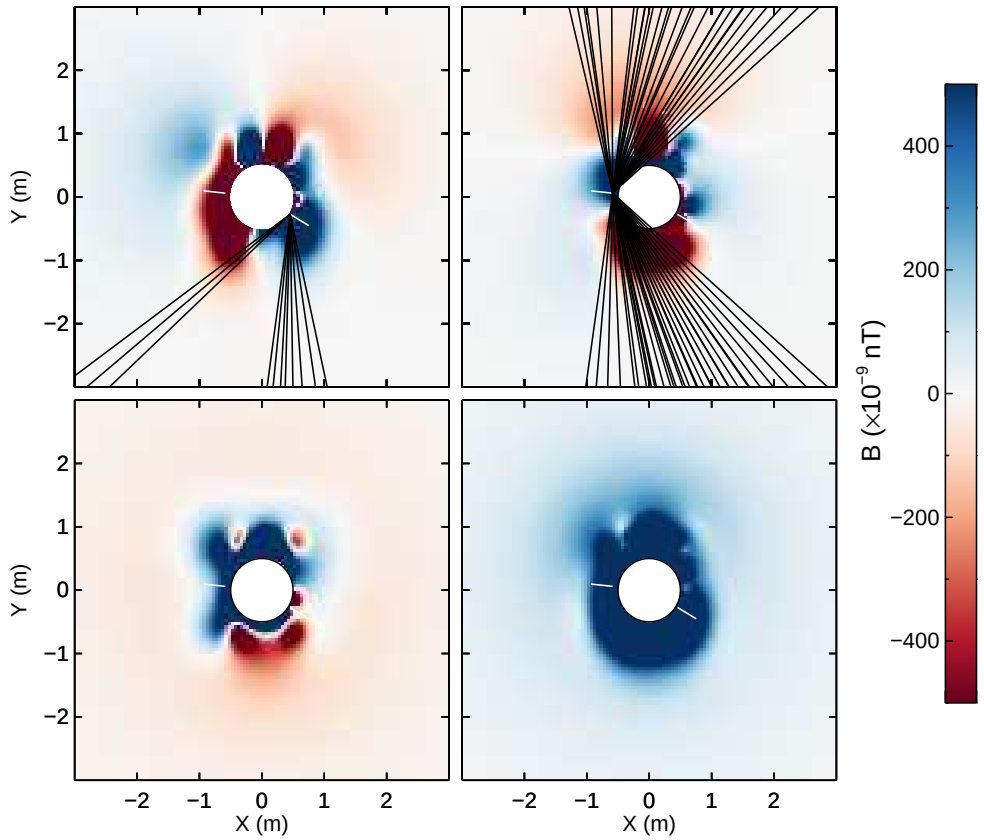

Figure 3. The strength of (counterclockwise from top left) the x, y, total, and z components of the magnetic field at z=0.50 m in the spacecraft-centered coordinate system where $+z$ points toward the Sun, $+x$ in the ram direction, and y completes the right hand set. The white circle at the center represents the cross section of our PSP model, the line extending down to the right represents the location of SPAN-A, and the line extending to the left represents the location of SPAN-B. The trajectories of the SPAN-Ae (top left) and SPAN-B (top right) that have been flagged for data quality are also shown.

were then combined into a single SPAN-E FOV. The total solid angle area on the sky of the individual and combined sensor FOVs were found by numerically integrating the area enclosd by these regions. To find the average FOV on the sky at each model potential (Figure 4), we assigned to each point on a 1°×1° grid a 1 if the point is contained within the sensor FOV, and a 0 if it is not. We then averaged these values over measured electron energy at each grid location to form a map of the percent transmission, or the fraction of the measurements which are capable of observing that region of the sky.

We show in Figure 5 the total FOV of SPAN-Ae, SPAN-B, and SPAN-E (SPAN-Ae and SPAN-B combined), averaged over measured kinetic energy, for each modeled potential. The FOV is shown as a fraction of 4π sr, although the actual FOV of the combined instruments is slightly smaller than 4π sr due to small gaps and overlaps between the two.

Without fields applied, (No E/B in Figure 5), SPAN-Ae (red line) sees approximately the same fraction of its ideal FOV (84%) as SPAN-B (87%). Inclusion of the fields affects the two sensor FOVs differently. The FOV of SPAN-Ae decreases to the next great-

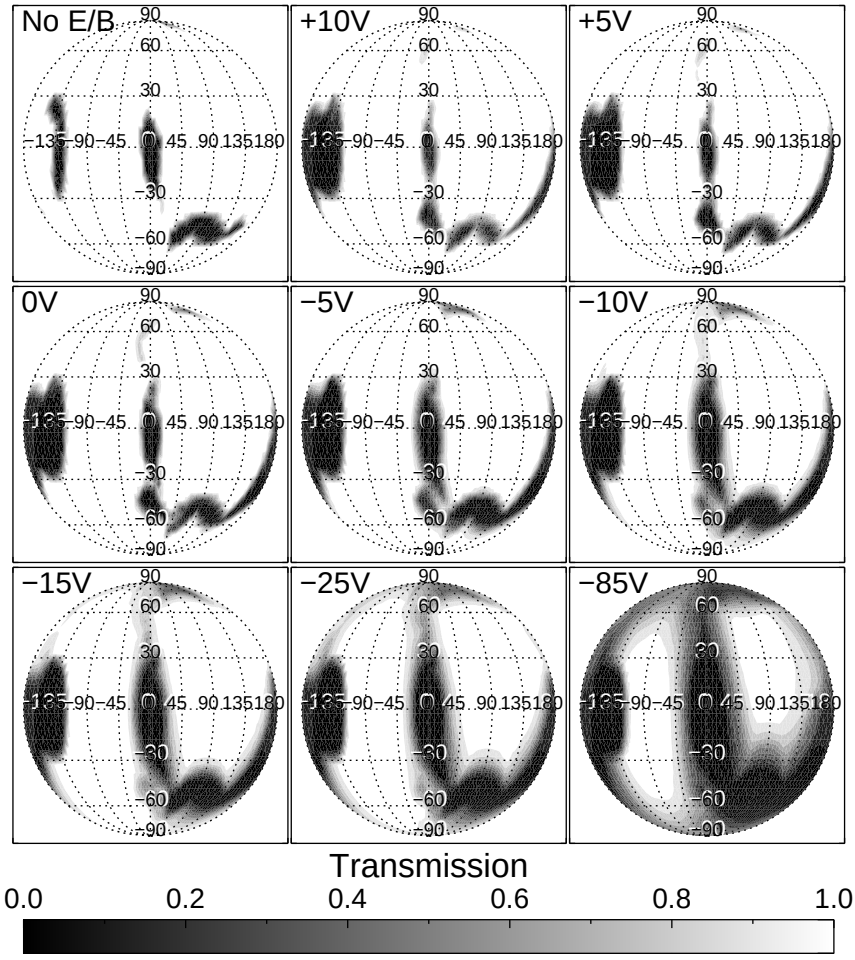

Figure 4. Energy-averaged FOVs of SPAN-E (SPAN-Ae and SPAN-B combined), represented as a percent transmission.

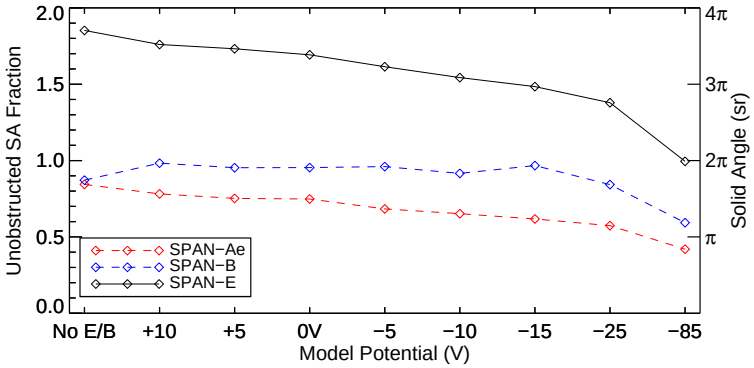

Figure 5. The fraction of the phase space solid angle measurable by SPAN-Ae and SPAN-B is shown as a percentage of the field of view at the aperture of each individual sensor. The observable SPAN-E (Ae and B combined) solid angle is shown as a fraction of 4π, averaged over all measured kinetic energies, for each spacecraft potential/magnetic field model.

est value (78%) in the +10V model, then decreases further as the potential becomes more negative. SPAN-B's FOV increases and remains roughly constant and roughly 20% greater than SPAN-Ae for all other models except the -25V and -85V. These trends at least partly mirror those in shown in Table 1: approximately similar numbers of both instruments' bins are blocked by the S/C in the No E/B model, while the total number of removed bins (blocked + flagged) is much greater for SPAN-Ae in all other models. Since Figure 5 incorporates the sheath focusing effect of the fields and the difference in sizes between coarse and fine resolution pixels, direct comparisons between the two is difficult.

4.3 Distribution Moment Measurements

The density, temperature, and velocity for each model, found by integration of the synthetic distribution function measurements, without any corrections for the effects of electrostatic and magnetic fields, are shown in Table 2. The accuracy of the measured density with respect to the model is shown as a percent error. To quantify the error in the multi-component quantities, we treat temperature and velocity as vector quantities, reporting a root-mean-square (RMS) error between the measured and model vector magnitudes (T and V) and the angle between measured and model vector directions (T_θ and V_θ). We find that the error in the density measurements ranges between 10-20% at spacecraft potentials $|\Phi_{SC}| \leq 25$V and increases as potential becomes more negative. At all potentials, the degree of temperature anisotropy is well preserved - the angle formed between the model and measured temperature vector orientation is $\lesssim$5 degrees at all models. The RMS error in the temperature magnitude decreases with potential from 8.92 eV at $\Phi_{SC} = +10V$ to 3.2eV at $\Phi_{SC} = -10V$, after which it increases to a maximum of 46.5eV at $\Phi_{SC} = -85$V. The RMS error in the velocity magnitudes is relatively larger - the $\sim$ 80kms^{-1} or more RMS observed is a considerable fraction of the 400 km s^{-1} bulk flow velocity of the model. Angular errors range from 10° to 23° and decrease as potential becomes more negative until the Φ_{SC}=-15V model is reached, from which they increase again up to the model with Φ_{SC}=-85V.

In general, errors in the measured quantities exist due to either incomplete or inaccurate sampling of the eVDF. Due to the limited energy measurement window (15 eV< E_a <510 eV) of our data sets (which is not necessarily the same as that of the actual SPAN detectors), as well as the eVDF energies not measurable at negative spacecraft potentials, our simulated SPAN-E detectors are unable to sample the eVDF across its full energy range. The resulting errors could be reduced by estimating the missing portion of the eVDF, e.g. by model fitting. We avoid doing this since the measurement errors caused by the warping of phase space and variable FOV occur purely in the angular dimensions and we wish to avoid any energy dependent modeling-related assumptions. To quantify the impact of our correction scheme, while also removing the effect of limited energy sampling, we compare the measured plasma moments to moments measured from a "perfect" measurement set which spans the same energy range with the same energy steps. These measurement sets do not have any S/C blockage or warping due to E/B fields and directly sample the eVDF at the same angular resolution as the combined, reinterpolated data (i.e. values of the energy flux have not been averaged over the solid angle area of the warped pixel). Since measurements of the plasma moments of these sets represent the best possible measurements by our simulated SPAN-E instruments, any additional error in the moments of our synthetic data sets must arise from incomplete or inaccurate sampling of the eVDF along its angular dimensions. The error in the uncorrected (top) and corrected (bottom) synthetic data set moments, with respect to the moments obtained from the "perfect" measurements are shown in Table 3. The density is quantified as a percent error; error in temperature and velocity magnitudes as an RMS, and between vector directions as an angle.

Across almost all models, using the particle tracing results as a correction reduces the error in the measurement of all plasma moments. Except for the density of the -25V

Table 2. Distribution function moments measured from the various electrostatic and magnetic field models. The top line (eVDF) represents the plasma properties far from the spacecraft. All remaining models (except No E/B) have the model magnetic field and the indicated spacecraft potential. Errors are relative to the plasma properties and are expressed as an absolute percent difference for density and for the remaining two moments as an RMS between component magnitudes and angle between vector directions.

Model	Density (cm^{-3})	Err (%)	T_x, T_y, T_z (eV)	RMS (eV)	T_θ (°)	V_x, V_y, V_z ($km\,s^{-1}$)	RMS ($km\,s^{-1}$)	V_θ (°)
eVDF	100.00	-	40.00 120.00 120.00	-	-	400.00 0.00 0.00	-	-
No E/B	91.20	8.80	42.28 116.01 113.12	1.53	4.78	419.62 -118.20 129.37	101.82	22.67
+10V	92.00	8.00	41.27 111.63 107.07	8.92	2.04	435.68 -105.00 91.15	82.91	17.71
+5V	91.25	8.75	41.97 113.73 108.88	7.45	2.06	464.98 -107.20 91.89	89.76	16.89
0V	89.83	10.17	42.58 116.35 111.07	5.76	2.03	486.59 -105.20 94.25	95.68	16.19
-5V	88.27	11.73	43.29 118.96 113.71	4.14	1.94	515.93 -89.78 88.17	98.78	13.71
-10V	86.47	13.53	44.17 121.78 116.82	3.20	1.82	556.76 -74.88 87.02	112.18	11.65
-15V	84.55	15.45	45.00 124.84 119.98	4.02	1.71	590.45 -60.12 97.29	128.26	10.96
-25V	81.20	18.80	47.35 131.07 126.22	8.48	1.69	614.79 -57.48 105.62	142.12	11.07
-85V	59.75	40.25	66.57 176.51 170.87	46.50	2.10	752.51 9.55 210.92	237.23	15.67

potential model, in which the density increases by a factor of ∼2, the error in density, temperature magnitude, and temperature angle decreases by an average of almost 60%. The improvement in the velocity moment accuracy is even greater; the errors decrease by $> 80\%$ on average in both magnitude and angle.

Table 3. Errors in uncorrected (top) and corrected (bottom) distribution function moments, compared to measurements of the undisturbed plasma far from the spacecraft, sampled at the same energy resolution and bounds.

Uncorrected	**No E/B**	**+10V**	**+5V**	**0V**	**-5V**	**-10V**	**-15V**	**-25V**	**-85V**
Density (%)	3.26	5.82	5.17	4.71	4.08	3.47	2.82	0.59	14.31
Temp. Mag. (eV)	1.83	2.68	2.82	3.00	3.16	3.24	3.42	4.30	12.31
Temp. Angle (°)	0.90	1.39	1.45	1.50	1.46	1.39	1.36	1.49	3.81
Vel. Mag. (km s^{-1})	101.31	83.22	88.85	92.43	91.54	99.62	110.69	116.10	175.33
Vel. Angle (°)	22.67	17.71	16.89	16.19	13.71	11.65	10.96	11.07	15.67
Corrected									
Density (%)	0.71	1.04	1.01	1.05	0.97	0.88	1.06	1.24	0.63
Temp. Mag. (eV)	0.97	1.14	1.20	1.17	1.16	1.21	1.30	1.26	2.80
Temp. Angle (°)	0.45	0.56	0.60	0.58	0.56	0.57	0.62	0.63	0.93
Vel. Mag. (km s^{-1})	13.22	11.49	14.20	11.04	10.97	12.33	12.24	16.22	69.17
Vel. Angle (°)	2.47	2.86	3.47	2.66	2.59	2.80	2.67	3.54	2.59

5 Discussion

The effect of our model electrostatic and magnetic fields on the FOV of the SPAN instruments can be thought of in terms of either how the data is collected (Section 4.1) or how it is to be interpreted (4.2). In the data, the variation in the FOV will appear as pixels receiving no or dimished electron energy flux. Kasper et al. (2016) provide anode/deflection maps for each instrument with overlays showing spacecraft blockage drawn from a detailed model of the PSP. These maps can thus serve as a useful point of comparison for our spaceraft model. Without fields, $\sim 11\%$ of the total number of SPAN-Ae's measurement bins are blocked. These lie mainly toward the anti-sunward facing angles (dark outline, Figure 2). Since these are not missing in the corresponding map in Kasper et al. (2016), our model likely overestimates the amount of blockage in this region. One possible explanation is that the actual bus of the PSP is hexagonal in shape, while in our model it is cylindrical.

If instead the cross section of the bus of our model is a hexagon circumscribed by the original circular cross-section (i.e. the vertices of the hexagon lie at $r = \sqrt{x^2 + y^2}$ =0.5m), the anti-sunward edge of the spacecraft is $r(1 - \sqrt{3}/2) = 6.7$ cm lower. If the SPAN-A detector is located radially outward from one hexagon face at the same $z = 0.156$m location, the instrument is able to see an extra $\theta = \arctan\left({}^{0.067}/_{0.156}\right) \approx 23.2°$ around the edge of the antisunward end of the spacecraft. This is approximately the angular width of the low-resolution anodes, so the greater number of pixels predicted to be blocked could at least partly be explained by the 2 dimensional cross-section of our model. The geometry of our model blocks an even greater fraction (~ 12) of SPAN-B's pixels, but this might not be as great of an overestimation; a large number of pixels are shown to be blocked in a similar region in Kasper et al. (2016). Fortunately, the field of SPAN-Ae is unobstructed at these angles.

The FOV of each instrument responds differently to the model fields, with SPAN-Ae the more sensitive of the two. The spacecraft magnetic field nearly doubles its blocked pixels and decreases its solid angle coverage by about 10%. While the number of blocked pixels of each is sensitive to spacecraft potential, the solid angle coverage of only SPAN-Ae seems to be sensitive to potential changes. Spacecraft potential in theory affects both of these quantities in opposite ways. From the point of view of our tracing simulations, electron trajectories bend towards the spacecraft on their way outwards from a positive potential. Conversely these trajectories bend away from negative potentials. Therefore, more blocked trajectories are expected at greater positive potentials, and less at greater negative potentials, as can be seen in Table 1. Pairs of adjacent trajectories which are not obstructed diverge at positive potentials, effectively increasing the spread of measurable velocity angles in a measurement pixel. At negative potentials, adjacent trajectories diverge, creating a smaller spread of measurable angles. We might therefore expect the fraction of the total solid angle of SPAN-B to decrease with increasingly negative spacecraft potentials in Figure 4, as it does for SPAN-Ae and E. However, the magnetic field is also capable of bending electron trajectories, and can do so in the opposite direction to that of the electric field.

Due to the spacecraft electrostatic and magnetic fields, the simulated measurements of a model eVDF (bottom panel, Figure 1) have obvious distortions when compared with the original eVDF (top panel). The element of phase space measured in the ambient plasma is at an angular location and/or covers a total solid angle area that is different than expected from instrument geometry. This warping of the FOV, along with FOV gaps and unmeasured low-energy portions of the spectra (for negative spacecraft potentials), leads to errors in the determination of eVDF moments. Both with and without correction, the errors in the temperature moments are relatively low across all models, both in magnitude and direction. As the second order moment of the distribution, its value is weighted more heavily towards the higher velocities/energies and therefore relatively less affected by the spacecraft fields, which have the biggest effect on low energy electrons. The velocity and temperature are successively less affected in this way, but are still sensitive to errors caused by the increasing amount of data cutoff by the negative Φ_{SC} values. If we compare the density moments to those from a "perfect" distribution spanning an identical energy range (thereby removing the error caused by missing data below $q\Phi_{SC}$), the errors in the density can be reduced to less than ∼5%. The model fields have the biggest impact on the velocity moments, and errors remain large (∼ 80-110km s^{-1}, or 20-28% in the magnitude, and ∼ 10-15° in angle).

In order to determine these moments, the data from SPAN-Ae and SPAN-B first needed to be resampled to uniform spacing in order to be combined into a single data set. Correcting the angular coordinates during the 2D interpolation yields a combined data set which is relatively free of the types of errors observed in the bottom panel of Figure 1. This correction, along with the second interpolation done to remove FOV gaps, reduces the errors in the distribution function moments in almost all models. The absolute improvement is small for density and temperature, but typically reduces errors by ∼ 50%. The velocity moment, which has the largest error in the raw data sets, is greatly improved on both a relative and absolute scale with these corrections.

6 Conclusion

During its mission, Parker Solar Probe (PSP) may develop a wide range of spacecraft potentials and will produce permanent magnetic fields near the SPAN instruments. Detailed modeling of the expected potential structure has been done several times for the PSP (Ergun et al., 2010), (Guillemant et al., 2012), and (Marchand et al., 2014). However, the effect of these fields on SPAN electron measurements is unknown, making the development of a correction scheme difficult. Our simplified approximation of the potential structure, while neglecting potentially important components such as the ion wake,

improves upon previous studies by combining a non-spherical potential with magnetic field components, and allows us to gain a first-order prediction of how the field of view and measurement accuracy of the SPAN detectors is affected by the fields around the spacecraft.

Our geometric spacecraft model alone blocks $\approx 11\%$ of the total number of measurement bins (all pixels at all measurement energies) of SPAN-Ae and $\approx 12\%$ of SPAN-B. Including the magnetic field alone does not affect the number of SPAN-B measurement bins blocked to ambient plasma electrons, but almost doubles the fraction of blocked SPAN-Ae bins. With the magnetic field and a positive spacecraft potential, the number of blocked bins increases and then decreases with negative potentials, with the fraction blocked dependent on the magnitude of the potential. Surprisingly, unlike SPAN-Ae and the combined instruments, the FOV of SPAN-B in velocity space is relatively unaffected by the spacecraft potential until the potential becomes less than -15V. We therefore conclude that the orientation of the field is such that its net effect is (from the viewpoint of our particle tracing simulations) to close more electron trajectories back onto the spacecraft or (from the plasma viewpoint) to scatter out of the instrument FOV electrons with certain velocity angles.

Without correcting for the gaps in the FOV, the missing portion of the eVDF at unmeasurable energies, or the angular warping due to the electromagnetic fields, errors ranged approximately 10-15% in the density moments, a few percent in the temperature, and 25% or more in the velocity. By accounting for any missing eVDF energies, we are able to reduce the errors in density and temperature by 50% or more; however, the velocity error remains high. We are able to greatly reduce these errors (to a few percent in magnitude and a few degrees in direction) by using the "true" look directions of the instrument pixels in the processing of SPAN-Ae and SPAN-B data into a single data set and by interpolating over the FOV gaps. Accurate velocity moments are especially important for the detection of weak shocks, the effects of the turbulent cascade, and the relative flow between electrons and ions.

This correction method could be implemented by compiling tables of "true" pixel look directions for a range of spacecraft potentials, and implementing corrections in the SWEAP data processing pipeline as data from SPAN-Ae and SPAN-B are combined into a merged SPAN-E data set. Whether the process is done by performing a two dimensional interpolation as discussed in this paper, or by another method, information about the look direction and angular coverage of each instrument pixel is needed (Section 3.2), which could either be the default values, or provided by the nearest entry in the table. The resulting corrected eVDF measurements could be offered as an additional data level 3 or 4 product (those which rely on ancillary data or are derived from calibrated data, (Korreck et al., 2014)). While our corrections are model dependent, and do not account for the negative potential ion wake ((Ergun et al., 2010), (Guillemant et al., 2012), and (Marchand et al., 2014)), they may still serve useful in their current form for improving the accuracy of measured plasma parameters, especially the bulk velocity. The technique presented in this paper provides a novel way of estimating and correcting for the effect of spacecraft fields on electron measurements, and its usefulness for the application to real data can be improved greatly with more realistic modeling.

Acknowledgments

We acknowledge the Parker Solar Probe project for support. The simulation results and the IDL codes used to produce them are available at https://doi.org/10.5281/zenodo.3333035.

References

Angelopoulos, V., Cruce, P., Drozdov, A., Grimes, E. W., Hatzigeorgiu, N., King,

D. A., ... Schroeder, P. (2019, jan). The space physics environment data analysis system (SPEDAS). *Space Science Reviews*, *215*(1). doi: 10.1007/s11214-018-0576-4

Dubouloz, N., Berthelier, J.-J., Malingre, M., Girard, L., Galperin, Y., Covinhes, J., ... Zinin, L. (1998). Thermal ion measurements on board interball auroral probe by the hyperboloid experiment. *Annales Geophysicae*, *16*(9), 1070–1085. doi: 10.1007/s00585-998-1070-1

Ergun, R. E., Malaspina, D. M., Bale, S. D., McFadden, J. P., Larson, D. E., Mozer, F. S., ... Wygant, J. R. (2010, July). Spacecraft charging and ion wake formation in the near-sun environment. *Physics of Plasmas*, *17*(7), 072903. Retrieved from `http://adsabs.harvard.edu/abs/2010PhPl...17g2903E` doi: 10.1063/1.3457484

Fox, N. J., Velli, M. C., Bale, S. D., Decker, R., Driesman, A., Howard, R. A., ... Szabo, A. (2016, December). The solar probe plus mission: Humanity's first visit to our star. Space Sci. Rev., *204*, 7-48. Retrieved from `http://adsabs.harvard.edu/abs/2016SSRv..204....7F` doi: 10.1007/s11214-015-0211-6

Garrett, H. B. (1981). The charging of spacecraft surfaces. *Reviews of Geophysics*, *19*(4), 577. doi: 10.1029/rg019i004p00577

Génot, V., & Schwartz, S. (2004, June). Spacecraft potential effects on electron moments derived from a perfect plasma detector. *Annales Geophysicae*, *22*, 2073-2080. Retrieved from `http://adsabs.harvard.edu/abs/2004AnGeo..22.2073G` doi: 10.5194/angeo-22-2073-2004

Guillemant, S., Génot, V., Matéo-Vélez, J.-C., Ergun, R., & Louarn, P. (2012, July). Solar wind plasma interaction with solar probe plus spacecraft. *Annales Geophysicae*, *30*, 1075-1092. Retrieved from `http://adsabs.harvard.edu/abs/2012AnGeo..30.1075G` doi: 10.5194/angeo-30-1075-2012

Guillemant, S., Genot, V., Velez, J.-C. M., Sarrailh, P., Hilgers, A., & Louarn, P. (2013, December). Simulation study of spacecraft electrostatic sheath changes with the heliocentric distances from 0.044 to 1 au. *IEEE Transactions on Plasma Science*, *41*, 3338-3348. Retrieved from `http://adsabs.harvard.edu/abs/2013ITPS...41.3338G` doi: 10.1109/TPS.2013.2246193

Hamelin, M., Bouhram, M., Dubouloz, N., Malingre, M., Grigoriev, S. A., & Zinin, L. V. (2002, March). Electrostatic interaction between interball-2 and the ambient plasma. 2. influence on the low energy ion measurements with hyperboloid. *Annales Geophysicae*, *20*, 377-390. Retrieved from `http://adsabs.harvard.edu/abs/2002AnGeo..20..377H` doi: 10.5194/angeo-20-377-2002

Isensee, U. (1977). Plasma disturbances caused by the HELIOS spacecraft in the solar wind. *Journal of Geophysics Zeitschrift Geophysik*, *42*, 581-589.

Johnstone, A. D., Alsop, C., Burge, S., Carter, P. J., Coates, A. J., Coker, A. J., ... Woodliffe, R. D. (1997).
Space Science Reviews, *79*(1/2), 351–398. doi: 10.1023/a:1004938001388

Kasper, J. C., Abiad, R., Austin, G., Balat-Pichelin, M., Bale, S. D., Belcher, J. W., ... Zank, G. (2016, December). Solar wind electrons alphas and protons (sweap) investigation: Design of the solar wind and coronal plasma instrument suite for solar probe plus. Space Sci. Rev., *204*, 131-186. Retrieved from `http://adsabs.harvard.edu/abs/2016SSRv..204..131K` doi: 10.1007/s11214-015-0206-3

Katz, I., Parks, D. E., Mandell, M. J., Harvey, J. M., Wang, S. S., & Roche, J. C. (1977). NASCAP, a three-dimensional charging analyzer program for complex spacecraft. *IEEE Transactions on Nuclear Science*, *24*(6), 2276–2280. doi: 10.1109/tns.1977.4329206

Korreck, K. E., Kasper, J. C., Case, A. W., Daigneau, P., Bookbinder, J. A., Larson, D., ... Marchant, W. (2014, aug). Solar wind electrons alphas and pro-

tons (SWEAP) science operations center initial design and implementation. In A. B. Peck, C. R. Benn, & R. L. Seaman (Eds.), *Observatory operations: Strategies, processes, and systems v.* SPIE. doi: 10.1117/12.2057314

Lai, S. T. (2011). *Fundamentals of spacecraft charging: Spacecraft interactions with space plasmas.* Princeton University Press. Retrieved from https://www.amazon.com/Fundamentals-Spacecraft-Charging-Interactions-Plasmas-ebook/dp/B0076LOQF6?SubscriptionId=AKIAIOBINVZYXZQZ2U3A&tag=chimbori05-20&linkCode=xm2&camp=2025&creative=165953&creativeASIN=B0076LOQF6

Lavraud, B., & Larson, D. E. (2016, September). Correcting moments of in situ particle distribution functions for spacecraft electrostatic charging. *Journal of Geophysical Research (Space Physics)*, *121*, 8462-8474. Retrieved from http://adsabs.harvard.edu/abs/2016JGRA..121.8462L doi: 10.1002/2016JA022591

Lewis, G. R., André, N., Arridge, C. S., Coates, A. J., Gilbert, L. K., Linder, D. R., & Rymer, A. M. (2008, May). Derivation of density and temperature from the cassini huygens caps electron spectrometer. Planet. Space Sci., *56*, 901-912. Retrieved from http://adsabs.harvard.edu/abs/2008P%26SS...56..901L doi: 10.1016/j.pss.2007.12.017

Mandell, M. J., Davis, V. A., Cooke, D. L., Wheelock, A. T., & Roth, C. J. (2006, October). Nascap-2k spacecraft charging code overview. *IEEE Transactions on Plasma Science*, *34*, 2084-2093. Retrieved from http://adsabs.harvard.edu/abs/2006ITPS...34.2084M doi: 10.1109/TPS.2006.881934

Marchand, R., Miyake, Y., Usui, H., Deca, J., Lapenta, G., Matéo-Vélez, J. C., ... Markidis, S. (2014, jun). Cross-comparison of spacecraft-environment interaction model predictions applied to solar probe plus near perihelion. *Physics of Plasmas*, *21*(6), 062901. doi: 10.1063/1.4882439

Rymer, A. M. (2004). *Analysis of cassini plasma and magnetic field measurements from 1-7 au* (Doctoral dissertation, University of London, University College London (United Kingdom). Retrieved from http://adsabs.harvard.edu/abs/2004PhDT.....139R

Salem, C., Bosqued, J.-M., Larson, D. E., Mangeney, A., Maksimovic, M., Perche, C., ... Bougeret, J.-L. (2001, oct). Determination of accurate solar wind electron parameters using particle detectors and radio wave receivers. *Journal of Geophysical Research: Space Physics*, *106*(A10), 21701–21717. doi: 10.1029/2001ja900031

Scime, E. E., Phillips, J. L., & Bame, S. J. (1994, August). Effects of spacecraft potential on three-dimensional electron measurements in the solar wind. J. Geophys. Res., *99*, 14. Retrieved from http://adsabs.harvard.edu/abs/1994JGR....9914769S doi: 10.1029/94JA00489

Song, P., Zhang, X. X., & Paschmann, G. (1997, February). Uncertainties in plasma measurements: effects of lower cutoff energy and spacecraft charge. Planet. Space Sci., *45*, 255-267. Retrieved from http://adsabs.harvard.edu/abs/1997P%26SS...45..255S doi: 10.1016/S0032-0633(96)00087-6

Whipple, E. C. (1981, November). Potentials of surfaces in space. *Reports on Progress in Physics*, *44*, 1197-1250. Retrieved from http://adsabs.harvard.edu/abs/1981RPPh...44.1197W doi: 10.1088/0034-4885/44/11/002

Figure 1.

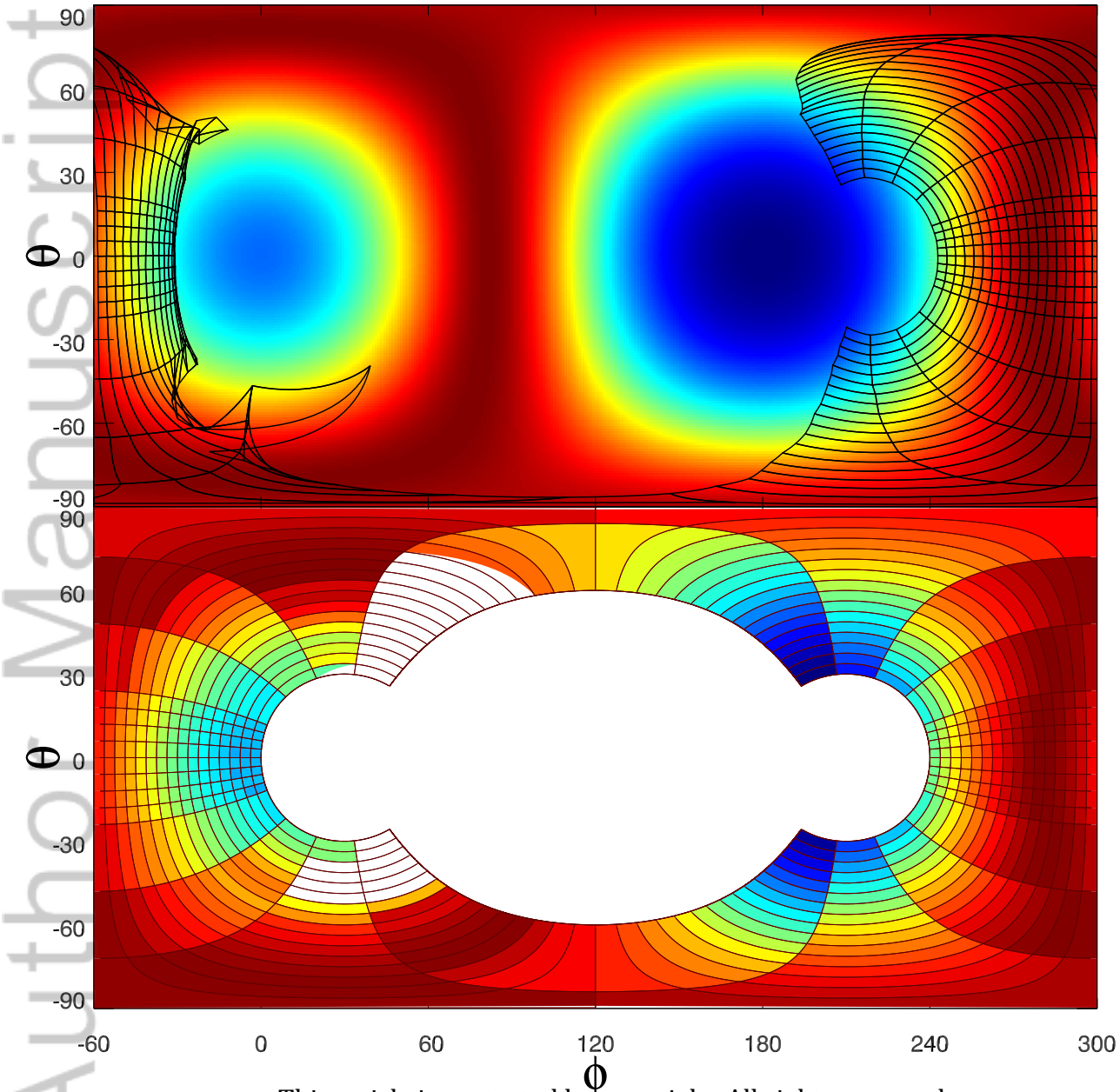

Figure 2.

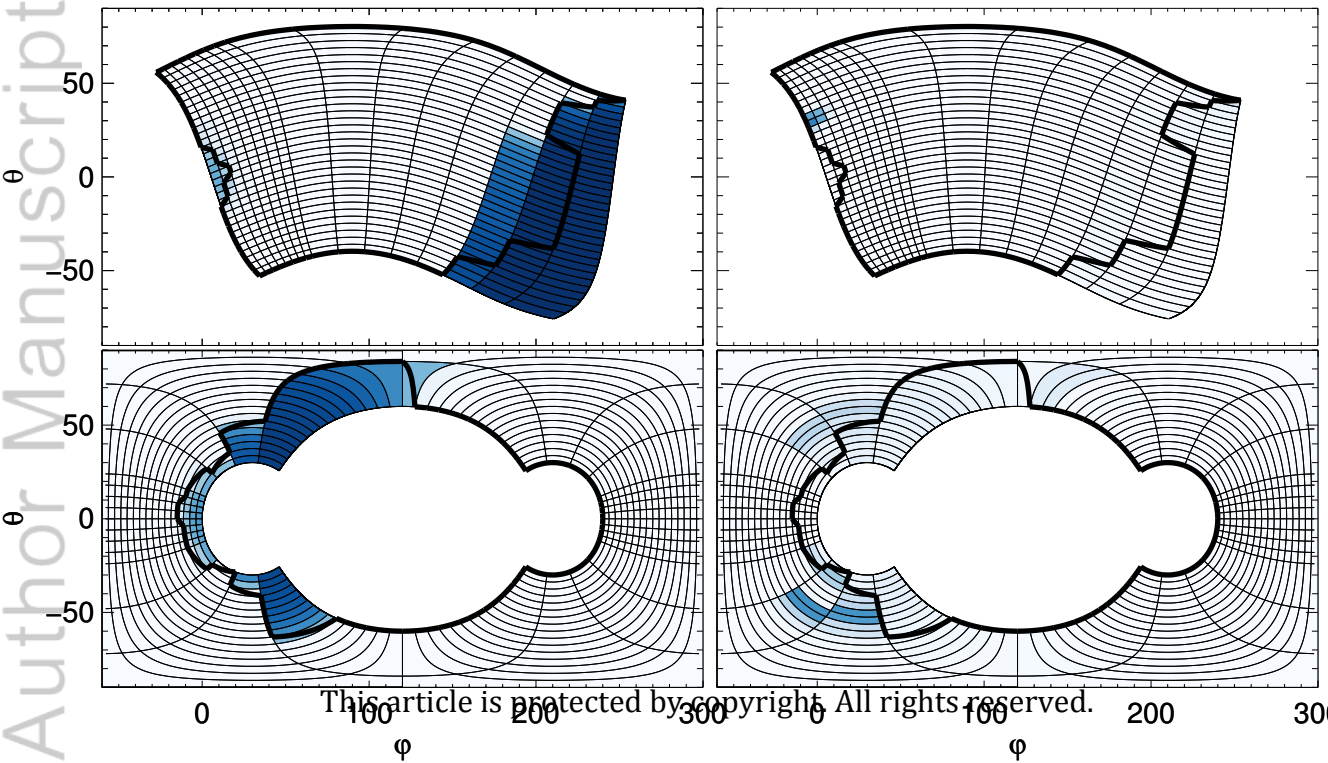

Figure 3.

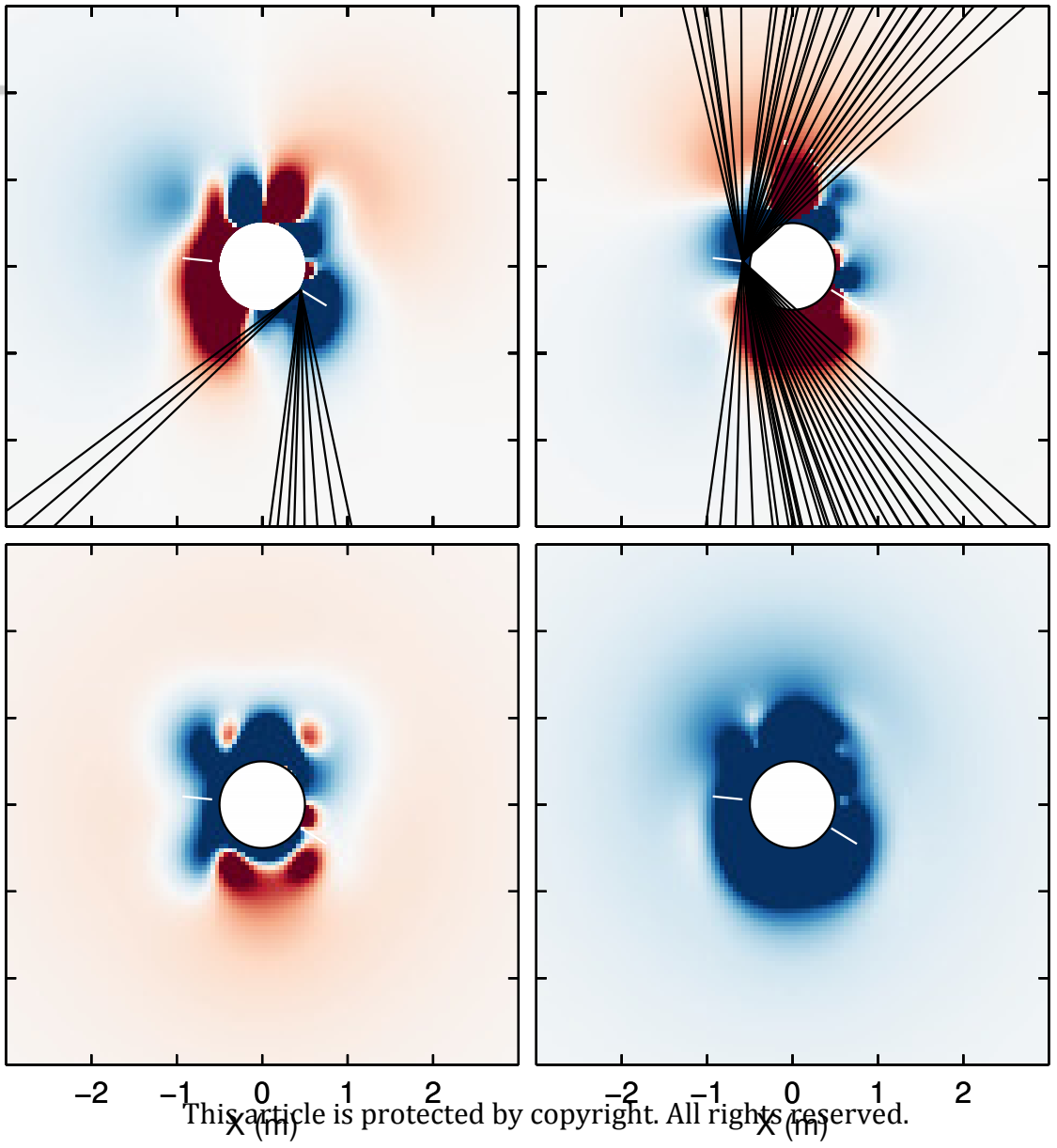

Figure 4.

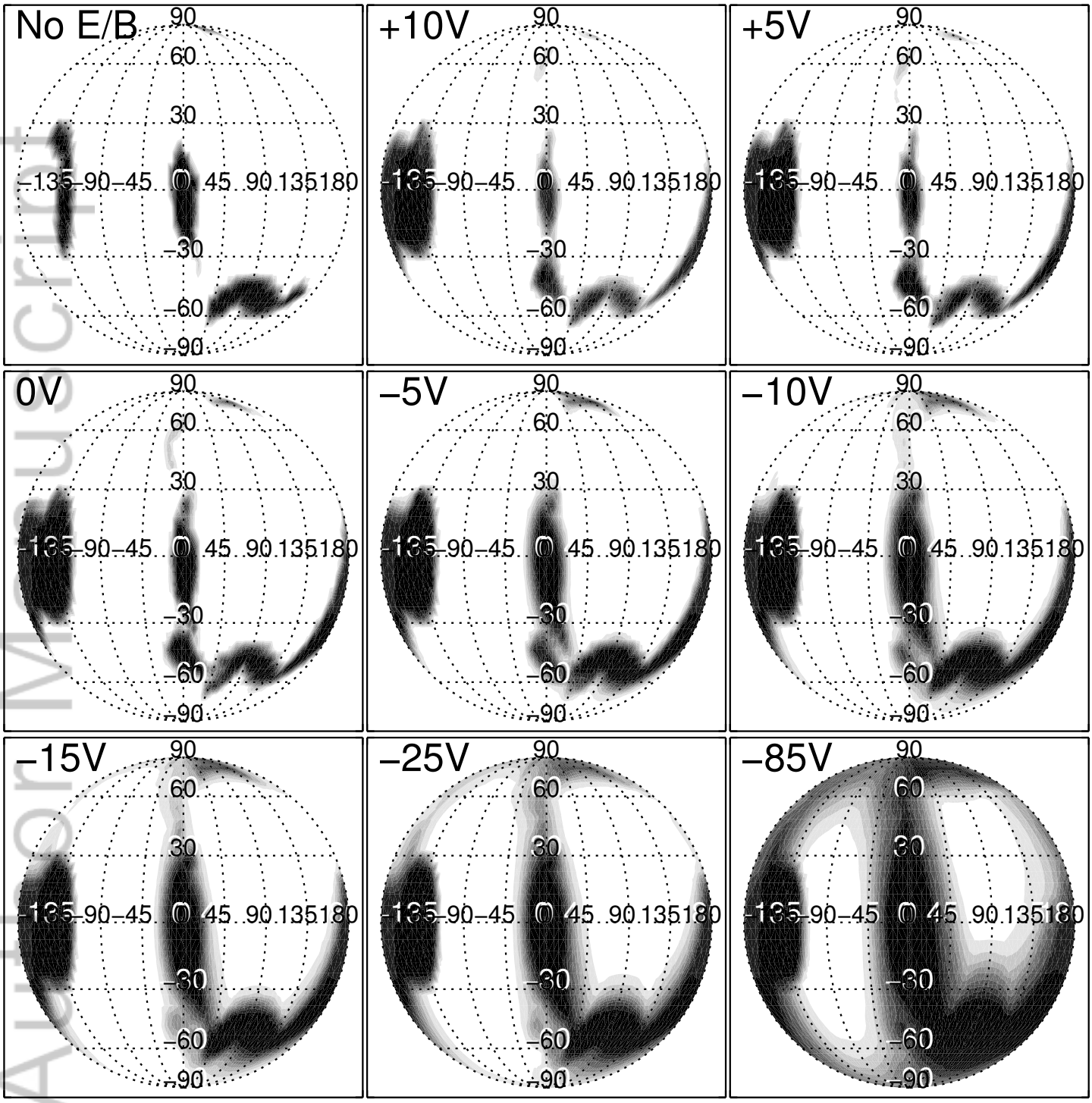

Figure 5.

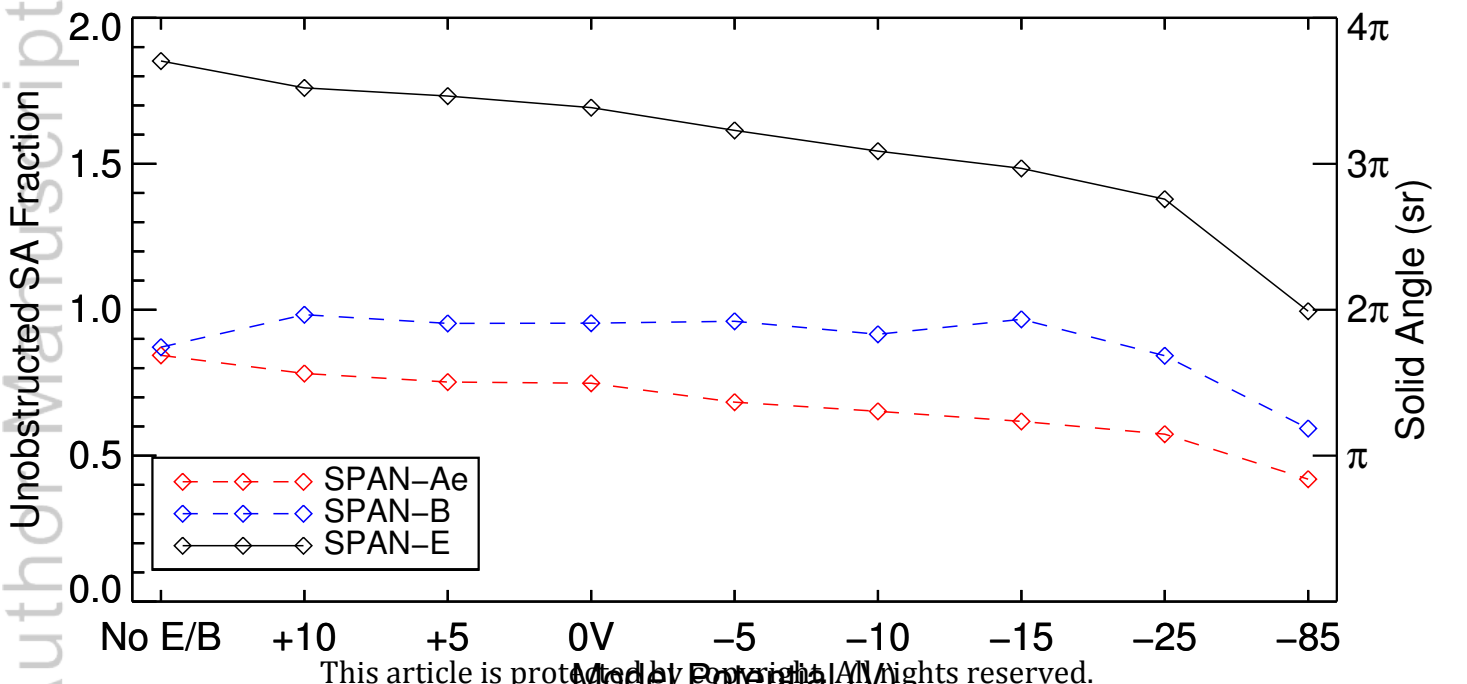

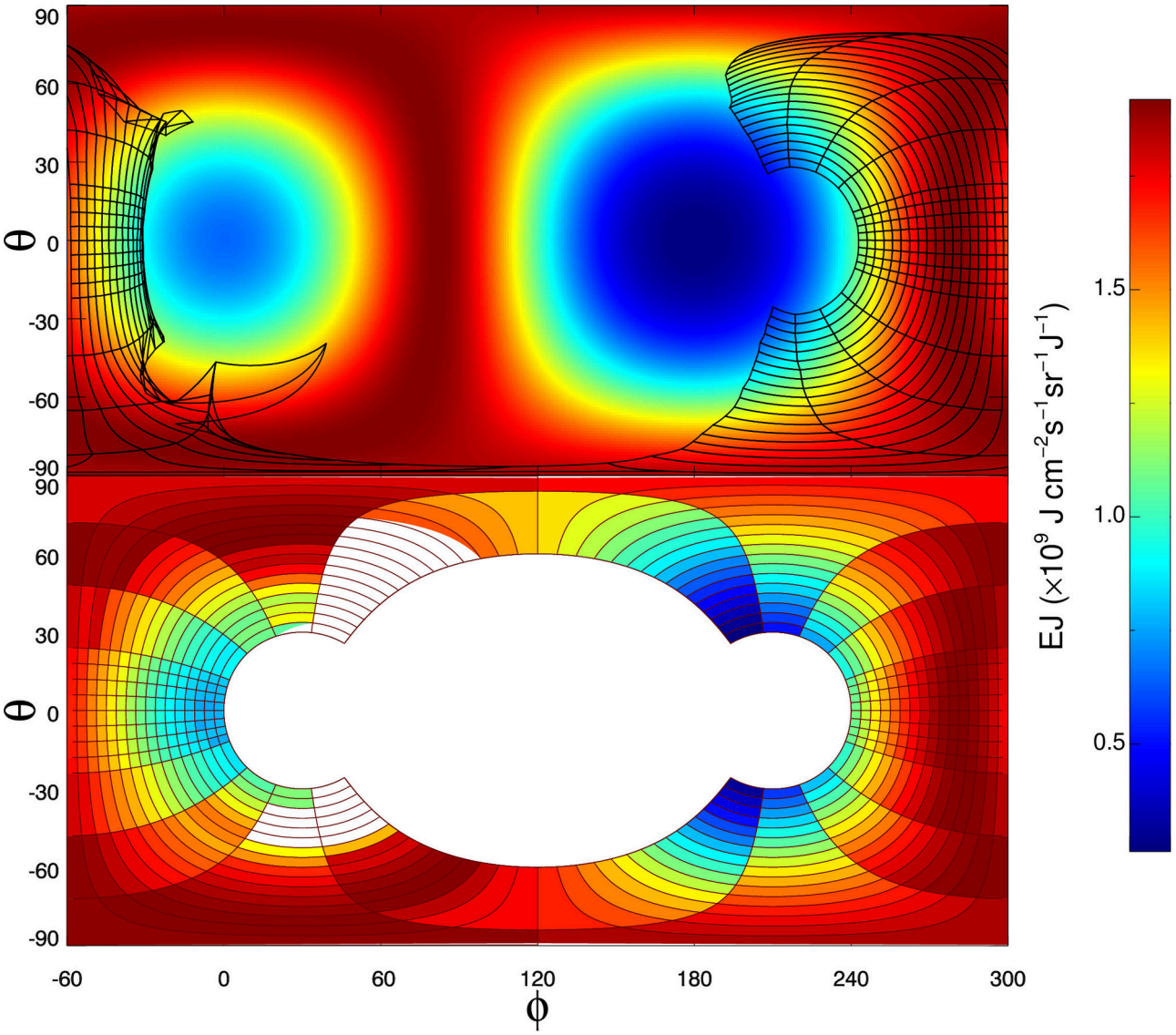

2019ja026823-f01-z-.eps

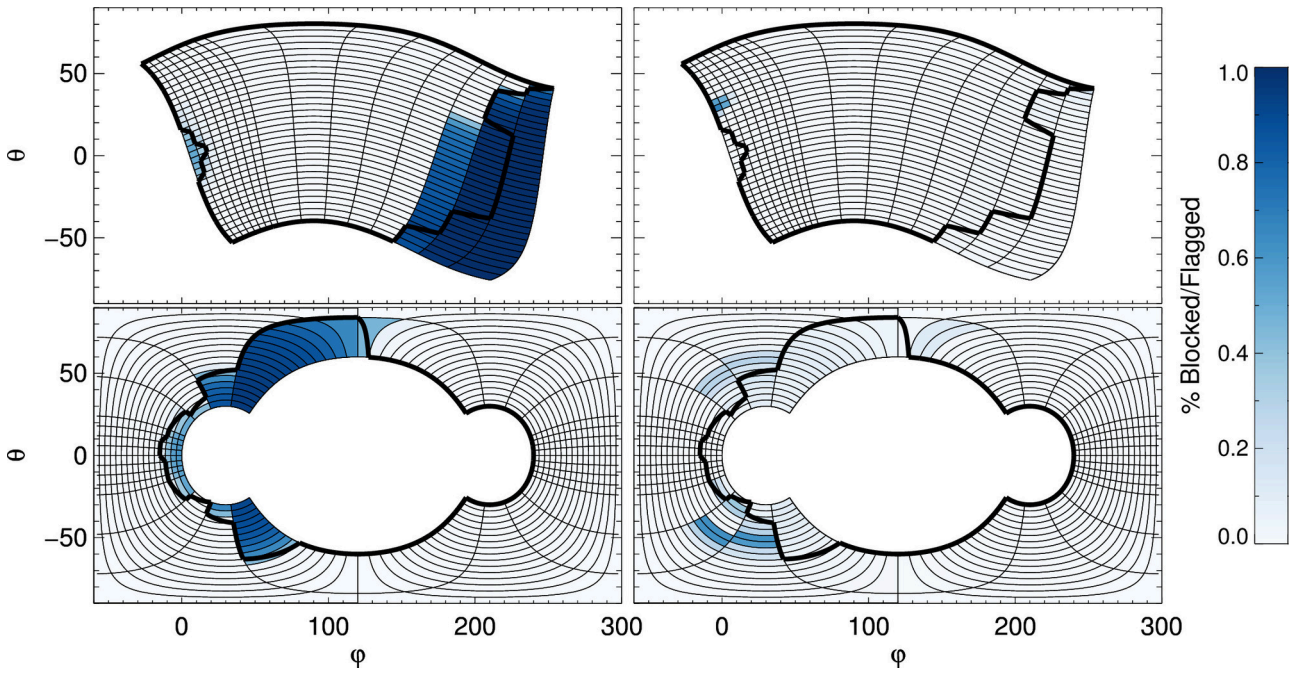

2019ja026823-f02-z-.eps

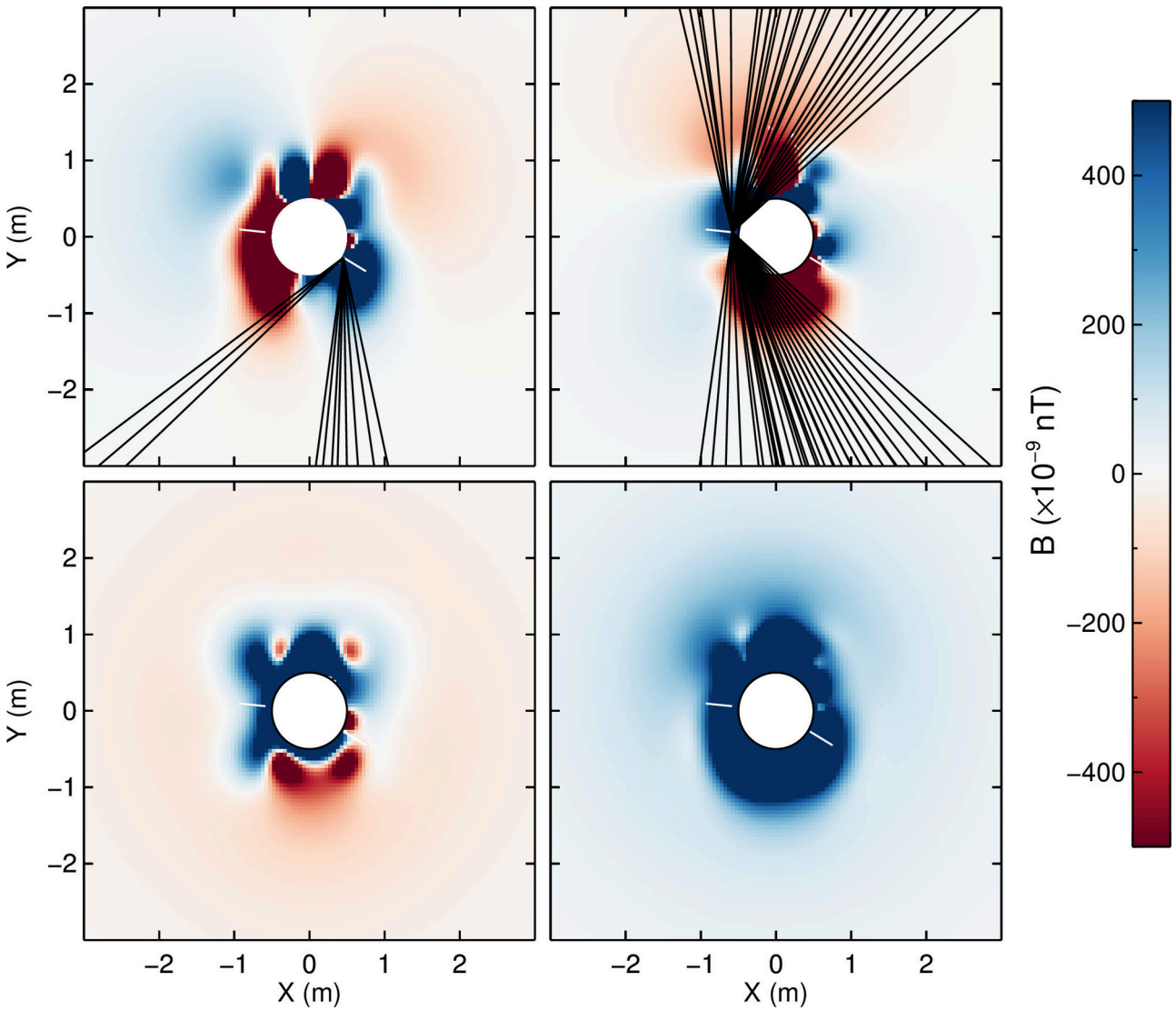

2019ja026823-f03-z-.eps

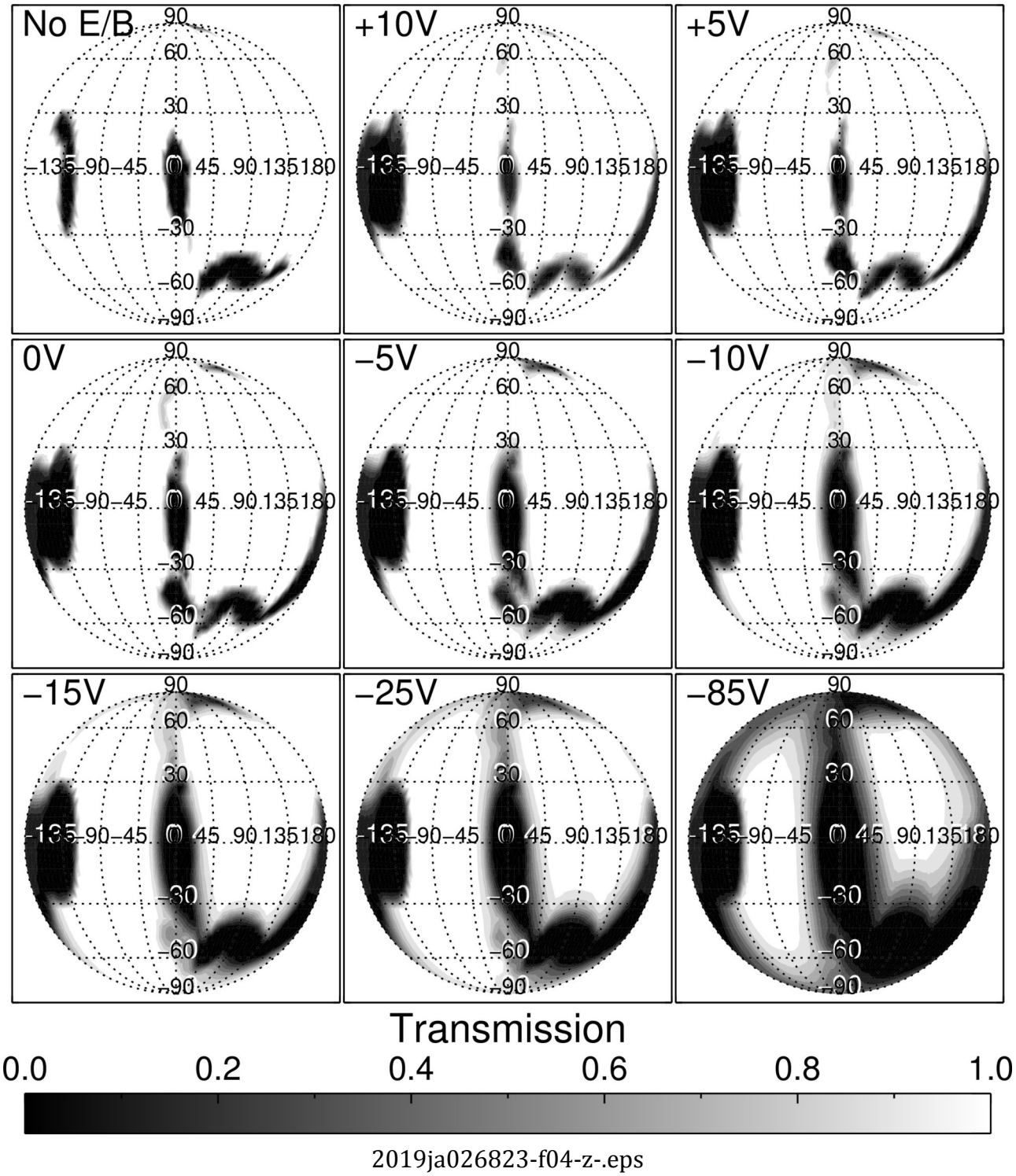

2019ja026823-f04-z-.eps

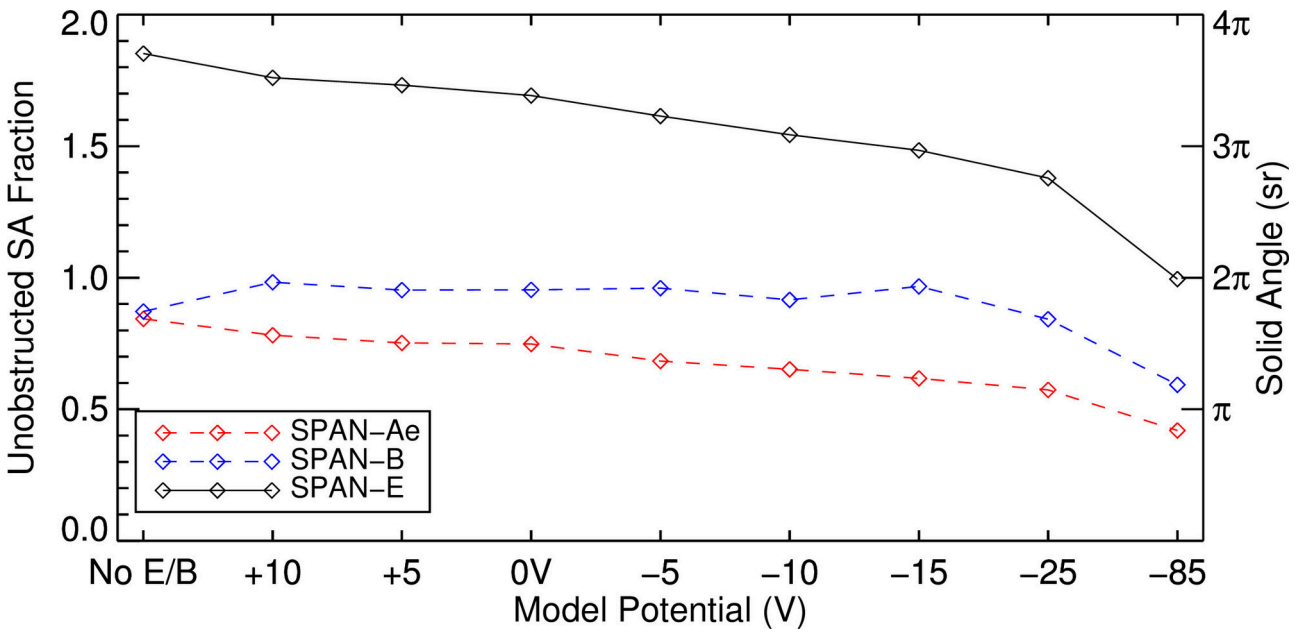

2019ja026823-f05-z-.eps